Alma Mater Studiorum · Università di Bologna

School of Science

Departement of Physics and Astronomy

Master Degree Programme in Astrophysics and Cosmology

STUDY OF MULTIPLE POPULATIONS IN TWO DYNAMICALLY YOUNG GLOBULAR CLUSTERS

Master Thesis

Presented by:
RICCARDO MAGNANI

Supervisor:
Dott. MARIO CADELANO

Co-Supervisor:
Ch.ma Prof. BARBARA LANZONI

Session V
Academic Year 2023/2024

"Science is a wonderful thing
if one does not have to earn one's living at it.
One should earn one's living by work
of which one is sure one is capable.
Only when we do not have to be accountable to anybody
can we find joy in scientific endeavour."
- Albert Einstein

Contents

1 Introduction

The traditional concept of globular clusters (GCs) as simple stellar populations, where all stars share the same age and abundances, is now a view of the past, as it has become clear that almost all GCs host significant abundance spreads within them. While all GCs show the same basic pattern, enriched populations in He, N, Na and populations depleted in O and C, the specifics of each cluster are unique.

Figure 1.1: HST image of Messier 5 (M5), one of the first studied GCs that showed chemical inhomogeneities (Osborn, 1971).

It is the manifestations of these distinctive chemical anomalies that cause the impressively complex colour-magnitude diagrams (CMDs) that have been uncovered with precision Hubble Space Telescope (HST) photometry, especially when viewed in the UV and near-UV (**Figure 1.2**). These star- to-star abundance variations within clusters are known as "multiple populations" (MPs, **Figure 1.3**). In particular, stars at the same magnitude along the RGB were found to display variations in the strengths of CH, CN, and NH blue absorption features, due to underlying star-to-star variations in C and N abundances. However, GCs also contain stars that are characterised by the same abundance pattern observed in field stars of the same metallicity. This has led to the notion that GCs are made up of MPs, one with field-like composition, and a second with "anomalous chemistry" unique to GCs.

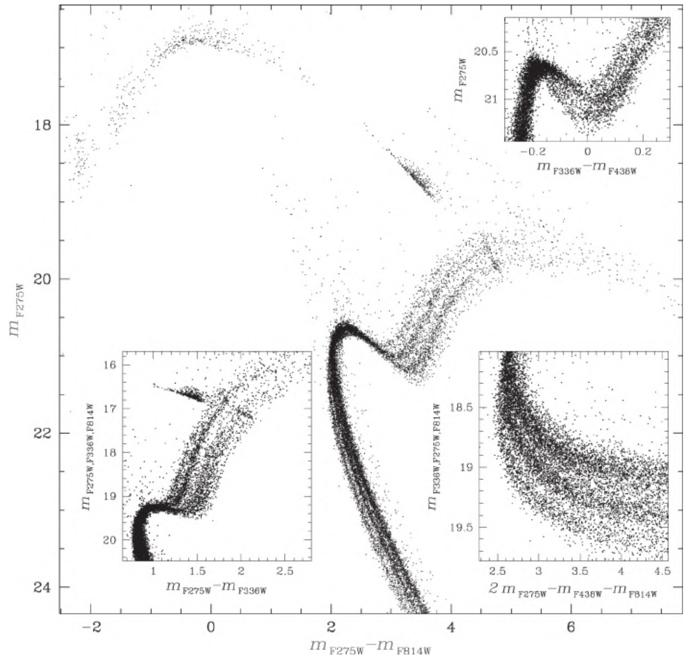

Figure 1.2: CMD of NGC 2808 using different HST colors.The inset CMDs highlight multiple sequences along the RGB, the MS, and the SGB (Milone et al., 2015).

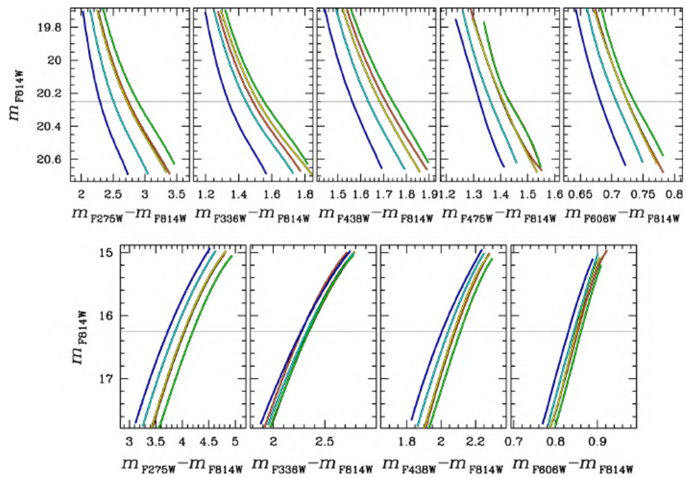

Figure 1.3: The green, orange, yellow, cyan, and blue lines are the MS (upper panels) and RGB (lower panels) fiducial lines for the five different populations in NGC 2808, at different HST colors (Milone et al., 2015).

At the beginning, when higher-resolution spectra allowed for direct spectroscopic measurements of Na and O (through atomic lines) in stars where N and C abundances were available, it was found that the N overabundance (C depletion) was associated to enhanced Na, hence O depletion (**Figure 1.4**). While O can potentially be depleted in the interiors of low mass stars through the CNO-cycle reactions, variations in the abundances of heavier elements like Na, Al, and Mg cannot by produced by fusion reactions within low-mass stars. Then, high-resolution photometry became capable of disentangle different stellar populations in RGB of CMDs.

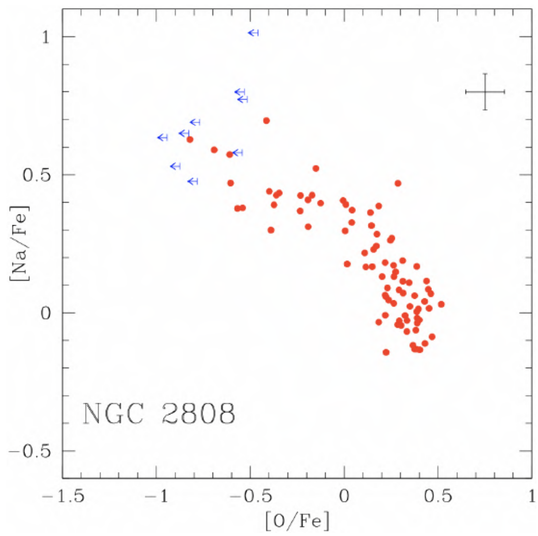

Figure 1.4: The Na-O anticorrelation in NGC 2808 using red giant stars (Carretta et al., 2006).

How material would then find its way into the low mass stars observed today is still an open question, as is the exact source of the material. Most models to date have adopted a scenario where material from a first generation of stars (FG or P1) pollutes the intra cluster medium out of which subsequent generations of stars were born (SG or P2). The light element variations span similar intervals in different evolutionary phases (Gratton et al., 2014). Observations show that unevolved stars on the MS and evolved RGB stars span the same ranges of chemical anomalies demonstrate that such light element variations cannot be due to accretion of processed material on already formed stars, as the anti-correlations would be strongly diluted by mixing as the stars evolve.

1.1 Origin of Multiple Populations

The precise scenario that create MPs in clusters is still discussed today. Every model in literature was developed with the aim to explain the observed chemical inhomogeneities in GCs and the mass budget of FG and SG stars, without abusing of fine tunings and exotic formation mechanisms.

1.1.1 AGB scenario

The model envisions the formation of a massive cluster with a single age and abundance pattern, representing a first generation of stars (FG). The feedback from high mass stars and the associated Supernovae (SNe) clear any remaining gas from within the cluster, hence all enriched material from the high mass stars and SNe are lost from the cluster. After 30 Myr, stars from the FG begin to evolve through the AGB phase of stellar evolution, and the winds of these stars, due to their low velocity, are not able to escape the cluster, so a reservoir of polluted gas begins to form in the cluster. This material cools and sinks towards the cluster centre, and once a critical density is reached a second generation (SG) of stars begins to form out of this material.
In order to reproduce the observed anti-correlations, this scenario requires the (re)accretion of large amounts of pristine material (i.e. material that shares the same abundances as

the FG stars) from the surroundings. This accreted material is then mixed with the AGB ejecta and forms SG stars, hence they would have different Na-O abundances ranging from the pure yields of AGB stars to those of the FG. One of the features of AGB stars that make them promising candidates to supply the enriched material is the fact that they can burn H at higher temperatures than main sequence massive stars. This allows them to activate the Al-Mg burning chain, hence to deplete Mg and increase Al.
However, this type of model has to deal with the fact that it can only produce a small fraction of the total cluster mass in 2G stars. This is due to the stellar Initial Mass Function (IMF) of the FG of stars, which only has a small fraction of its total mass in stars in a specific mass range that can produce material to pollute/enrich the 2G of stars. In order to obtain the observed fractions of primordial and enriched stars the model needs to assume that GCs lose substantial fractions of their initial population of stars, often up to 95% of their initial masses while retaining all/most of the SG stars.

1.1.2 Fast Rotating Massive Stars and Interacting Binaries

Massive stars also undergo hot hydrogen burning in their cores, during the MS, and as such are also potential candidates to provide the enriched material needed to form MPs. However, as this happens deep within the stars it is difficult to bring up the enriched material to the stellar surface where it can be released into the GC intra-cluster medium. Massive stars that are rapidly rotating can overcome this problem, due to rotationally induced mixing which can cause, in extreme cases, the stars to be (nearly) fully mixed. Decressin et al. (2007) developed a scenario using Fast Rotating Massive Stars (FRMS) as the enrichment source (**Figure 1.5**). This scenario is similar to that of the AGB scenario, using the enriched material from a FG of stars to form a SG, but happens when the cluster is much younger (< 10-20 Myr). As in the AGB scenario, the ejecta of FRMS must also be diluted to match the observed abundance patterns. However, since the cluster is still young there is no need to bring the material from outside the cluster, as it is assumed that the cluster has retained a relatively large fraction of gas/dust left over from the formation of the FG. The winds of the FRMSs then mixes with the left over gas and forms a SG of stars. The FRMS scenario suffers from the same mass budget problem discussed for the AGB scenario. FRMS naturally produce a Na-O anti-

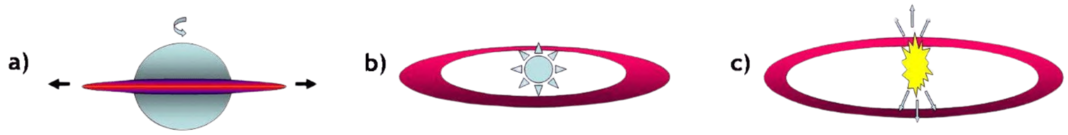

Figure 1.5: Schematic view of the FRMS scenario showing the possible geometry of the stellar ejecta at various evolutionary phases: a) in MS the star rotates near or at the critical velocity, matter is preferentially ejected in the equatorial plane by the action of the centrifugal acceleration; b) after the MS, the surface velocity is no long critical and the isotropic wind is triggered mainly by radiation; c) the SNe explosion may favor ejection through jets aligned along the rotational axis.

correlation and the enriched material can also be strongly enhanced in He. FRMS are not able to activate the Al-Mg chain before the end of the MS, so are not able to explain the observed Mg spreads in some clusters without ad-hoc changes to the nuclear cross sections. Charbonnel et al. (2014) presented a variant on the FRMS scenario in order to solve the mass budget problem. Here, the FG stars forms with a top heavy stellar IMF (i.e., only stars that would not be alive today) and the SG stars would be mainly low mass stars. In this model, stars with "primordial composition" would be actually second generation stars that formed primarily from material left over from the first generation. Another way to release enriched material from the cores of massive stars into the intra-cluster medium is through binary interactions. de Mink et al. (2009) modelled a binary interaction between a 20 and 15 $M_\odot$ star and investigated the yields of the expelled material. They found that the 20 $M_\odot$ star shed about 10 $M_\odot$ worth of material due to the interaction, and that the yields matched the observed trends in GCs. While the overall trends and correlations of the yields should apply to most massive stars, the exact yields depend on a number of parameters, e.g., the time of interaction (i.e. stellar evolutionary state), total mass of the stars and the mass ratio of the stars. Hence, interacting binaries have the benefit of potentially explaining the observed variations from cluster to cluster, but have difficulty matching the discreteness of abundance ratios found in many sub-populations. A potential problem of scenarios that operate in the first few Myr of a cluster's life, is that after 3-8 Myr (depending on the cutoff mass for SNe), core collapse SNe begin to explode. The retention of just a small amount of this material will result in Fe spreads that are in conflict with observations.

1.1.3 Early Disc Accretion scenario

Bastian et al. (2013) suggested an alternative model for MPs that did not invoke multiple epochs of star-formation. Instead, the model used the enriched material ejecta from high-mass interacting binary stars (de Mink et al., 2009) as well as the FRMS within the cluster to pollute low mass stars that formed at the same time as the high mass stars. The authors suggested that low-mass ($< 2\ M_\odot$) stars may retain the protoplanetary discs around them for 10 Myr which would sweep up the enriched material as they passed through the cluster core (the authors also assumed that the cluster is mass-segregated from a very early age, so that the high mass stars are concentrated in the cluster centre). The enriched material that was swept up by the discs would then eventually be accreted onto the host star. This scenario requires that the accreting stars are fully convective (in order to mix the accreted material throughout the star) which in turn means that the accretion timescales are extremely short (1-3 Myrs). This minimises the time that mechanism could potentially work which effectively limits the amount of processed material that can be supplied and accreted.

Hydrodynamical simulations found that while the disc did indeed accrete material from the ISM, the accreted material had little or no angular momentum which caused the disc to rapidly accrete onto the star and disappear. Without the disc no further accretion would be possible. The authors found that this happened on a rapid timescale, $\sim 10^4$ years, much shorter than the required 10^7 years for the scenario to work.

1.1.4 Turbulent separation of elements during GC formation

Hopkins (2014) also put forward a potential origin of MPs that did not invoke multiple generations of star-formation within GCs. In his scenario, MPs would be the result of cloud physics during the earliest phases of GC formation. In extremely turbulent environments, like those in progenitor clouds of GCs, large dust grains can become aerodynamic and begin to move separately from the gas and small dust grains. Large resonant fluctuations in the dust can then develop. Within these overdense regions, dust will be over-represented, so any stars that form within such regions will be enhanced in the elements associated with large dust grains. On the other hand, the gas and small dust grains (like Fe grains) will be more uniformly distributed. In principle, this mechanism provides a natural and powerful way to separate elements in the early phases of GC formation. Since this mechanism depends on the level of turbulence, it would predict larger abundance spreads in more mass proto-GC clouds, consistent with observations. However, Na and O normally occur on the same dust grains, so such fluctuations would predict a Na-O spread but as a correlation instead of the anti-correlation seen in GCs. Also, He is not affected by dust, so an additional mechanism would need to be invoked to explain the inferred He spreads in GCs. Finally, any enhancement in an element in some stars would necessarily lead to a depletion of that element in other stars. The expectation is that, starting from field star abundance composition, more or less symmetrical spreads around the field star abundance would be present. Observations, however, show the scatter in a single direction from the position of where halo field stars lie (at a given metallicity).

1.1.5 Reverse Population Order for GC formation scenarios

In order to alleviate the mass-budget problem, some authors tentatively investigated formation models where the abundances of forming stars move from P2 to P1, as star formation within the cluster proceeds. The scenario outlined Marcolini et al. (2009) describes GC formation from gas enriched locally by a single Type Ia SN and AGB yields superimposed on an ambient medium pre-enriched by low-metallicity Type II SNe. The star formation of the proto-GC only takes place inside this region and stars born within the inner volume will be depleted in O and Mg (because of the single SN Ia) and enhanced in N, Na and Al abundances (due to AGB pollution). External to this volume can be found a region with the same composition as the proto-halo gas at the epoch of GC formation. After a new generation of stars is born, associated SNe II begin to pollute and expand the inner volume, while mixing with the lower metallicity material from the external shell. Hence, the [Fe/H] and the CNO sum remain constant during cluster evolution and the N-C and Na-O anti-correlations can be reproduced. The Al-Mg anti-correlation can only be reproduced assuming that AGBs produce more Al than predicted by models (by a factor of $\sim$10-50). Nonetheless, the dynamical feasibility of the scenario has not been probed with hydrodynamical simulations and severe assumptions need to be made on the Fe content of the ISM at the epoch of formation, as well as the the size of the inner region where the inhomogeneous pollution by the SN Ia and AGBs is confined. More importantly, this class of models require very peculiar stellar configurations that are not expected at the present epoch.

1.1.6 Extended cluster formation event

Elmegreen (2017) have further explored a model that invokes the special conditions of galaxies or Giant Molecoluar Clouds (GMC) at high redshift (namely high density, turbulence and pressure environments) to foster the formation of MPs before the first SNe occurs ($<$ 3 Myr). Here, a first generation of stars is born in the core of a massive,

dense and turbulent GMC. Due to the high stellar densities, high mass stars have their envelopes stripped (and rotating massive stars lose large parts of their envelopes through decretion discs) very rapidly, which (as discussed above) are expected to show many of the observed abundance anomalies. This material mixes with that left over from the formation of the FG and forms subsequent generations. Low mass FG stars are assumed to be ejected due to two mechanisms, the first is binary dynamics and the second is that the gravitational potential of the cloud core/cluster is rapidly varying as the gas within it (which dominates the potential) is moved due to stellar feedback. It remains to be seen if the high FG mass loss rates (and low SG mass loss rates) required are feasible.
Wünsch et al. (2017) have suggested that the winds released from massive stars can become so dense in a massive and dense young cluster, that they enter a catastrophic cooling regime and can collapse into the cluster centre. Here, the material may mix with left over primordial material (i.e. dilute) and form a second generation of stars. Hence, this is another mechanism (rather than stellar interactions) that can potentially make enriched material from massive stars available for further epochs of star-formation within a cluster. This also suffers from the mass budget problem and would require large fractions of FG stars to be lost.
A key aspect of this scenario is that it happens (and terminates) before the first SNe occurs within the proto-GC in order to avoid Fe spreads (similar to the FRMS scenario). One potential problem with the scenario is that it takes high-mass stars some time to increase their He mass through nuclear burning, whereas this model starts using stripped material from the massive stars at $t = 0$. This may be ok for standard clusters with small He spreads but it may be difficult to reproduce clusters that hosts a large He spread.

1.1.7 Very massive stars due to runaway collisions

Gieles et al. (2018) have developed a model for MPs that adopts Very Massive Stars (VMS, > 103 M$\odot$) as the origin of the processed material. In this model, the proto-cluster undergoes adiabatic contraction due to gas accretion, increasing the stellar density and subsequently the stellar collision rate. A runaway collision process can form a VMS burning processes through its stellar wind into the intra-cluster environment. This processed material mixes with pristine gas and forms further generations of stars until the very massive stars burns out, or potentially explodes due to instabilities within the star. Because the VMS can be continuously rejuvenated through stellar collisions, the amount of processed material ejected by the star can be several times the maximum mass of the star. While this process leads to multiple generations of stars within the cluster, the expected age spread would be less than $\sim$3 Myr.
One major advantage of this model is that it predicts a super-linear scaling between the mass of the very massive star and the mass (or density) of the cluster. This naturally produces the observed trend of increasing fractions of enriched stars (and potentially as well as the increasing spreads in N, Na, etc) as a function of GC mass. One of the major drawbacks of the model is that VMSs are still only theoretical, although numerical simulations were performed showing that under certain conditions (relevant for GC formation) runaway collisions are likely to take place, even when considering two-body relaxation and the strong stellar mass loss of the massive object due to its stellar wind. This same process is expected to also be at work in clusters today, if they reach the required stellar densities.

1.1.8 Accretion of substellar companions

Winter and Clarke (2023) presented a novel mechanism for late delivery of pollutants into stars via accretion of substellar companions. In this scenario, stars move through a medium polluted with AGB and massive star ejecta, accreting material to produce companions with typical mass ratio $q \sim 0.1$. These companions undergo eccentricity excitation due to dynamical perturbations by passing stars, culminating in a merger with their host star. The accretion of the companion alters surface abundances via injected pollutant. Alongside other self-enrichment models, the companion accretion model can explain the dilution of pollutant and correlation with intracluster location. The model also explains the ubiquity and discreteness of the populations and correlations of enrichment rates with cluster mass, cluster age, and stellar binarity. Abundance variations in some clusters can be broadly reproduced using AGB and massive binary ejecta abundances from the literature. In other clusters, some high companion mass ratios ($q \geq 1$) are required. In these cases, the available mass budget necessitates a variable degree of mixing of the polluted material with the primary star, deviations from model ejecta abundances, or mixing of internal burning products.

1.1.9 Transient Overcooling in the Early Universe

The last scenario, which is still under study, was proposed by Renzini et al. (2022). By selecting massive interactive binaries as the most suitable formation scenario, to avoid supernova contamination the authors endorsed the notion that above a critical mass stars fail to produce supernova events, but rather eventually sink into black holes without ejecting much energy and heavy metals. This assumption has the attractive implication of suppressing star formation feedback for some 5-10 Myr, in practice leading to runaway star formation, analog to overcooling that in absence of feedback would have turned most baryons into stars in the early Universe. Under such conditions, multiple episodes of stars formation, incorporating binary star ejecta from previous episodes, appear to be unavoidable, thus accounting for the ubiquity of the multiple population phenomenon in globular clusters. If this is the way GCs formed, then such a delayed feedback is likely to play a role in star formation. In particular, it would boost the star formation efficiency in dense regions, perhaps helping the formation of nuclear clusters and more.
In this proposed scenario, a few observational facts still remain unaccounted. This is the case for the presence of Li and/or some heavy s-process elements (such as Ba) in a few SG stars, especially among the red-sequence stars of Type II clusters. Li and s-process elements have been traditionally taken as the smoking gun for the intervention of AGB stars. As red-sequence stars in Type II GCs experienced Fe enrichment from SNe, over $\sim$10 Myr after the formation of FG, they may as well have included ejecta from massive AGB stars that started to enrich the ISM another $\sim$20 Myr after the beginning of supernova explosions. This tentative solution is a bit contrived, but so complex is the overall multiple population phenomenon that some apparently minor detail may need a specific fix.

1.2 Structural and Kinematical properties of MPs

The kinematical and structural properties of MPs can provide key insights into the early epochs of GC evolution and formation. In fact, one of the predictions of MP formation models is that SG stars form a centrally segregated stellar sub-system possibly characterized by a more rapid internal rotation than the more spatially extended FG system. Although the original structural and kinematical differences between FG and SG stars are gradually erased during GC long-term dynamical evolution, some clusters are expected to still retain some memory of these initial differences in their present-day properties. Indeed, sparse and inhomogeneous observations show that MPs are characterized by quite remarkable differences in their relative structural parameters/radial distributions, different degrees of orbital anisotropy, different rotation amplitudes and significantly different binary fractions.
In order to examine these differences using a solid representative sample, Dalessandro et al. (2019) studied the spatial distributions of MPs in a sample of 20 globular GCs spanning a broad range of dynamical ages. The differences between FG and SG stars were measured by means of the parameter A^+ introduced by Alessandrini et al. (2016) and Lanzoni et al. (2016). This parameter is calculated as the area enclosed between the cumulative radial distributions of FG and SG stars, ϕ_{FG} and ϕ_{SG}, respectively:

$$A^+(R) = \int_{R_{min}}^{R} (\phi_{FG}(R') - \phi_{SG}(R'))dR' \tag{1.1}$$

where R is the distance from the cluster center. With such a definition, a more centrally concentrated SG yields negative values of A^+. By construction A^+ depends on the considered cluster-centric distance and therefore a meaningful cluster-to-cluster comparison requires that the parameter is measured over equivalent radial portions in every system. The authors were able to provide the first purely observational evidence of the dynamical path followed by MPs from initial conditions toward a complete FG-SG spatial mixing. Less dynamically evolved clusters have SG stars more centrally concentrated than FGs, while in more dynamically evolved systems the spatial differences between FG and SG stars decrease and eventually disappear. By means of an appropriate comparison with a set of numerical simulations, these observational results are consistent with the evolutionary sequence expected by the long-term dynamical evolution of clusters forming with an initially more centrally concentrated SG sub-system (**Figure 1.6**). This scenario is further supported by the evidence of a inverse trend between A^+ and the stage of GC dynamical evolution inferred by the ratio between the present-day and the initial mass of the cluster. Indeed, this ratio provides a measure of the evolutionary stage of a cluster and its degree of mass loss due to two-body relaxation. The data show that clusters with small value of mass ratio, hence systems that lost a larger fraction of their original mass, tend to have their MPs spatially mixed.
Overall, this study provides a global view of the evolution of the MP structural properties. They lend support to an interpretation of the different degrees of spatial mixing observed in various clusters in terms of dynamical evolution of systems in which the SG formed more centrally concentrated than the FG. At the same time, the empirical evolutionary sequence found in the analysis also provides a key constraint for models exploring the long-term dynamics of MPs, which is an important aspect of the study of MP clusters.

This scenario has important implications also for the interpretation of other kinematical features observed in MPs, such as their rotation patterns and anisotropy profiles, and therefore is key to shed light on the physical initial conditions that brought to the formation of MPs.

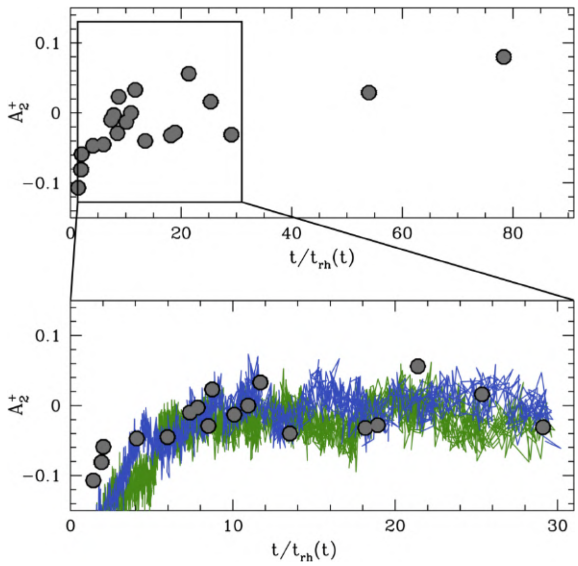

Figure 1.6: Upper panel: distribution of A^+ as a function of N_h=t/t_{rh} (ratio between the cluster age t and its current half-mass relaxation times t_{rh}) for all the clusters in the sample. Bottom panel: zoom on the distribution of cluster with N_h< 30. Results from N-body models are overplotted to the observations. Blue and green curves represent models starting with an SG 5 and 10 times more centrally concentrated than FG, respectively. Plot taken from Dalessandro et al. (2019).

An opposite scenario was proposed by Leitinger et al. (2023), based on a homogeneous and wide-view analysis of multiple stellar populations in 28 Galactic GCs. By using a combination of HST photometry together with wide-field, ground-based photometry the authors were able to analyse between 84% and 99% of all stars in each cluster. **Figure 1.7** shows the resulting A^+ parameters as a function of dynamical age. They found that dynamically old clusters all have $A^+ \sim 0$, in agreement with the idea that due to relaxation, populations become mixed. This also agrees with the findings of Dalessandro et al. (2019). In dynamically young clusters, a larger range of A^+ values was found. Surprisingly, there are not only centrally concentrated P2 populations ($A^+ < 0$) consistent with the findings of Dalessandro et al. (2019), but also clusters with centrally concentrated P1 populations ($A^+ > 0$), and clusters with full spatially mixed populations ($A^+ \sim 0$) in the same small dynamical age range (N_h< 4.5).
Centrally concentrated primordial populations were found in NGC 3201 ($A^+ = 0.46 \pm 0.12$) and NGC 6101 ($A^+ = 0.70 \pm 0.13$). In the former one FG stars had the highest concentration at intermediate radii around 150 arcsec, with SG stars being dominant in the outer parts and also towards the centre of the cluster. Statistical tests showed that the central concentration of SG was significant at a $\sim 2\sigma$ level and significant at the 8σ level towards the outer parts, leading to a U-shaped distribution in the relative fraction of SG stars. NGC 6101 was studied also by Dalessandro et al. (2019), which categorised it as a mixed GC with parameter $A^+ = -0.003 \pm 0.001$.

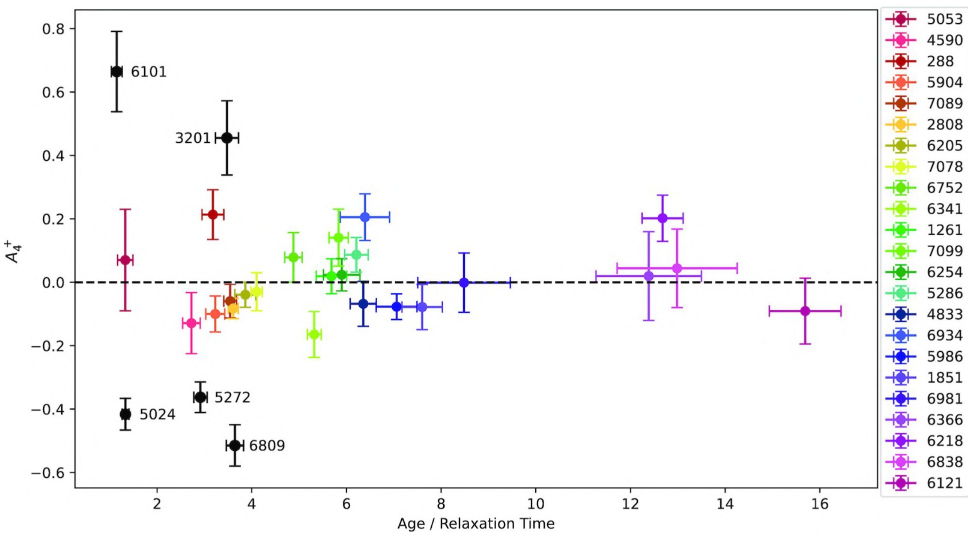

Figure 1.7: The total cumulative radial distributions in terms of the A^+ parameter for the 28 Galactic GCs as a function of their dynamical age. Using a common radius limit for comparison, clusters with an A^+ value greater than 3σ significance from zero are displayed as labelled black points. An A^+ value close to zero indicates the MPs are spatially mixed throughout the analysed spatial extent of the cluster. Significantly positive A^+ values indicate that the primordial (FG) population is more centrally concentrated, while negative values indicate the enriched (SG) population is more centrally concentrated. Plot taken from Leitinger et al. (2023).

On the contrary, Leitinger et al. (2023) show that the cluster cumulative radial distribution, combining HST and ground-based photometry, indicate a centrally concentrated primordial population. The existence of clusters born with centrally concentrated primordial (and homogeneously mixed) populations exacerbates the mass-budget problem facing many cluster formation scenarios. The diversity in these results also highlights the need for additional theories that can account for the wide variety of initial conditions.
At this point, there are two different scenarios in contrast between each other. Focusing on NGC 3201, which shows strong positive A^+ value in Leitinger et al. (2023) analysis, Cadelano et al. (2024) demonstrated the validity of Dalessandro et al. (2019) scenario. They used NGC 3201 as instructive case and presented a detailed morphological and kinematic characterization of its MPs, based on a combination of photometric and astrometric data. The U-shaped distribution of SG stars already described by Leitinger et al. (2023) is actually a bimodal distribution, significantly more centrally concentrated than the FG within ~1.3 cluster's half-mass radius. Beyond this point, the SG fraction increases again, likely due to asymmetries in the spatial distributions of the two populations. **Figure 1.8** shows the cumulative radial distribution of MPs. Results are in good agreement with those reported by Leitinger et al. (2023) and this figure clearly shows why the value of A^+ is positive. While this result would in general correspond to a FG more centrally concentrated than the SG, the structural configuration of this cluster is actually more complex. As shown in the inset panel, within the half-mass radius there is an opposite pattern: SG stars are more centrally concentrated than FG stars in the central region. This result is confirmed also by the binned radial distribution of the ratio between the number of SG stars ($N_{\rm SG}$) to the total number of stars ($N_{\rm TOT}$) as a

function of cluster-centric distance as shown in the lower panel of **Figure 1.8**. In fact, such a distribution shows a puzzling bimodal behaviour, in agreement with the results previously reported by Leitinger et al. (2023).

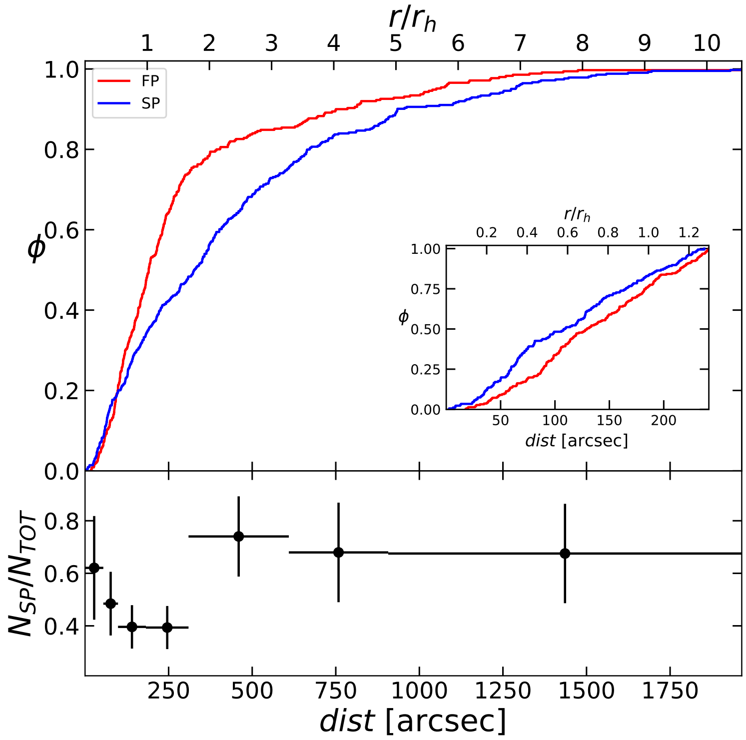

Figure 1.8: Cumulative radial distribution and number ratio of MPs. Top panel: cumulative radial distribution of the FG (red curve) and SG (blue curve). The inset panel shows the cumulative distribution of stars within the cluster half-mass radius. Bottom panel: ratio between N_{SG} and $N_{\mathrm{TOT}} = N_{\mathrm{FG}} + N_{\mathrm{SG}}$ calculated in different radial bins. Plot taken from Cadelano et al. (2024).

This interpretation is supported by the key information provided by the MP kinematic properties. Indeed, it was found that the FG is isotropic across all the sampled cluster extension, while the velocity distribution of the SG becomes radially anisotropic in the cluster's outer regions, as expected for the dynamical evolution of SG stars formed more centrally concentrated than the FG (**Figure 1.9**). The combination of spatial and kinematic observations provide key insights into the dynamical properties of this cluster and lend further support to scenarios in which the SG forms more centrally concentrated than the FG, as the one presented by Dalessandro et al. (2019).

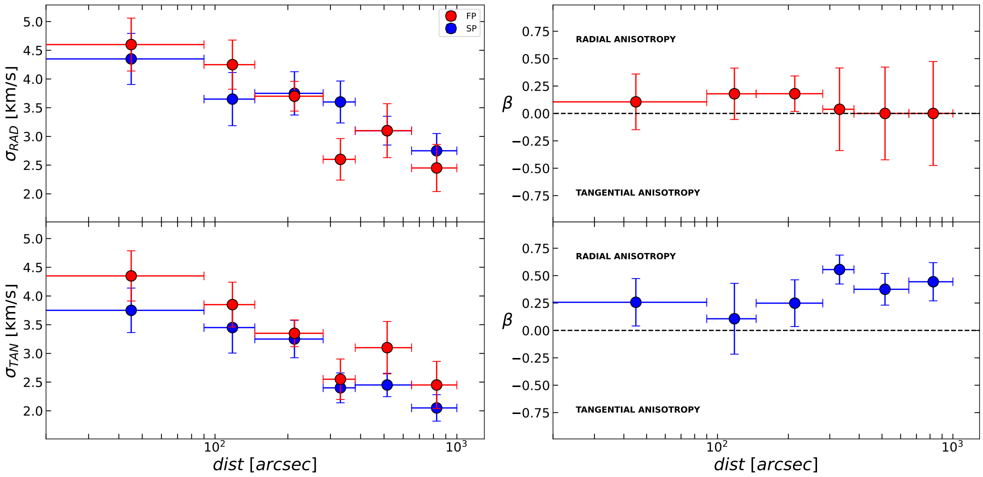

Figure 1.9: Velocity dispersion and anisotropy profiles of the MPs in NGC 3201. Left-hand panel: radial and tangential dispersion profiles are presented in the top and bottom panels, respectively. Red and blue points are obtained for FG and SG stars, respectively. Right-hand panel: anisotropy profiles for the FG and SG stars in the top and bottom panel, respectively. Plot taken from Cadelano et al. (2024).

The study of the kinematic properties of FG and SG stars can provide key insights into the formation and dynamical history of MPs. In order to investigate this correlation between dynamical age and kinematic of MPs, Dalessandro et al. (2024) presented the first 3D kinematic analysis of MPs in a representative sample of 16 GCs. For each GC in the sample authors studied the MP Line Of Sight (LOS), plane-of-the-sky and 3D rotation as well as the velocity distribution anisotropy. The differences between FG and SG kinematic patterns were constrained by means of parameters specifically defined to provide a global measure of the relevant physical quantities and to enable a meaningful comparison among different clusters. This analysis provided the first observational description of the MP kinematic properties and of the path they follow during the long-term dynamical evolution. In particular, evidence of differences were found between the rotation of MPs along all velocity components with the SG preferentially rotating faster than the FG. The difference between the rotation strength of MPs is anti-correlated with the cluster dynamical age. These differences are larger for dynamically young clusters and they become progressively indistinguishable as dynamical evolution proceeds (**Figure 1.10**). Observations attest that FGs are characterized by isotropic velocity distributions at any dynamical age probed by sample. On the contrary, the velocity distribution of SG stars is found to be radially anisotropic in dynamically young clusters and isotropic at later evolutionary stages (**Figure 1.11**). The comparison with a set of numerical simulations shows that these observational results are consistent with the long-term evolution of GCs forming with an initially more centrally concentrated, rapidly rotating SG subsystem.

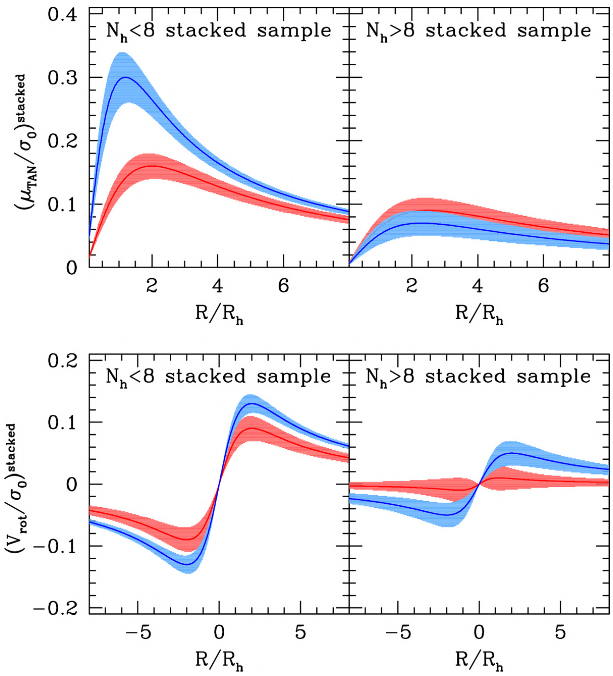

Figure 1.10: Best-fit results of the kinematic analysis of the dynamically young ($N_h < 8$) and old ($N_h > 8$) stacked samples. FG is in red and SG in blue. The lower panels refer to the LOS rotation, while the upper row shows the results for the Tangential velocity component. Plot taken from Dalessandro et al. (2024).

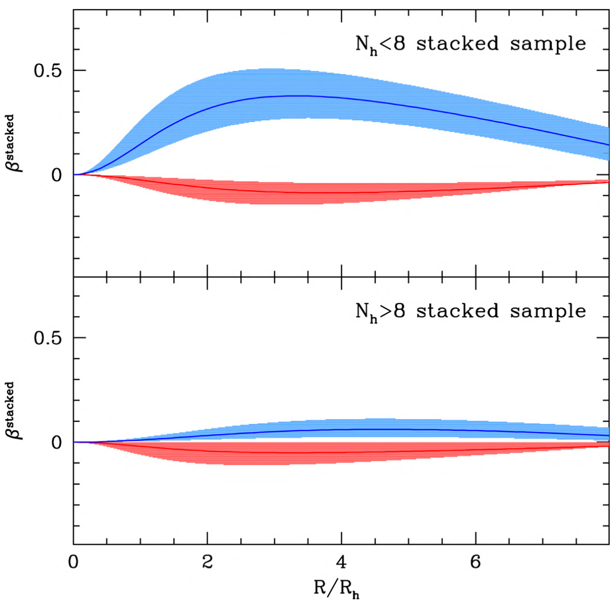

Figure 1.11: Best-fit results of the anisotropy analysis of MPs in the two stacked samples. The upper panels shows the best-fit anisotropy profiles of the FG (red) and SG (blue) sub-populations as obtained for the stacked sample of dynamically young GCs, while the lower panel refers to dynamically old systems. Plot taken from Dalessandro et al. (2024).

In this scenario, the structural properties of dynamically young systems (i.e. those with $t/t_{rh} < 3$-4) are particularly meaningful, as they are expected to be only partially affected by long-term dynamical evolution and therefore retain better memory of the conditions emerging from the formation and early evolutionary phases. As a consequence, the study of dynamically young clusters can allow us to probe the early structural properties of MPs, thus better defining their dynamical evolutionary path. The key constraints provided by this analysis have also important implications on the interpretation of the other MP kinematical features that are becoming observable now thanks to Gaia and the high multiplexing capabilities of state of the art multi-object and integral field unit (IFU) spectrographs.
Therefore, the validity of Dalessandro et al. (2019) scenario can be tested by studying the spatial distribution of MPs in dynamical young GCs. In particular, the possible finding of SG stars more concentrated in the cluster center would be a solid proof in favor of this scenario. The key problem is that literature offers very few studied cases of dynamically young GCs with centrally concentrated SG (e.g., see **Figure 1.12** from Onorato et al., 2023). Hence, this thesis has the aim to expand this sample by studying two dynamically young clusters, NGC 5053 and NGC 5466, in order to offer a stronger statistical validation to Dalessandro et al. (2019) scenario.

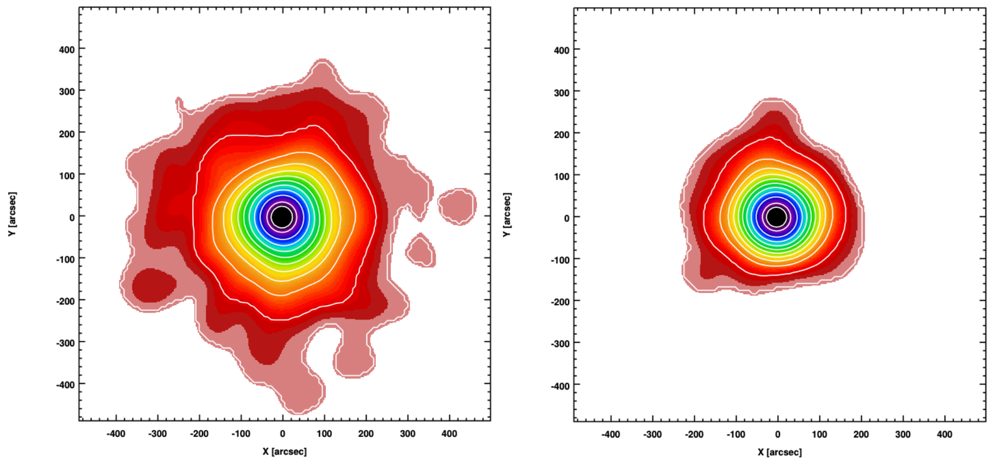

Figure 1.12: Onorato et al. (2023) studied NGC 2419, which is the GC with the lowest dynamical age in the Galaxy (N_h=0.28). 2D density maps and isodensity contours of the FG and SG (in the left and right panels, respectively) clearly show SG stars more centrally concentrated than FG stars.

2 NGC 5053

NGC 5053 is a metal-poor GC ([Fe/H]=-2.29 dex) located near the north Galactic cap ($l = 336°$, $b = 79°$) with a Galactocentric radius of $R_{GC} = 17.8$ kpc and 17.4 kpc far from the Sun. Near NGC 5053, 500 pc away based on the X, Y and Z positions from Harris (1996) (2010 version) is NGC 5024 (M53). Using SDSS photometry, Lauchner et al. (2006) discovered a 6° tidal tail associated with NGC 5053. A study by Chun et al. (2010) detected a tidal bridge-like structure between NGC 5053 and its neighbour M53. If this bridge-like structure is genuine, it suggests that the evolution of NGC 5053 has been influenced not only by the Galaxy, but also through interactions with M53. With a mass $M=6.3 \cdot 10^4$ $M_\odot$ and a cluster central density ρ_c=3.3 $M_\odot/pc^3$ (Baumgardt et al., 2023), NGC 5053 is a low-density and low-mass cluster compared with the mean values of other GCs. It is a dynamically young GCs since $N_h=t/t_{rh}=1.5$, due to an estimated age $t=12.5 \pm 2.0$ Gyr (Arellano Ferro et al., 2010) compensated by a half-mass relaxation timescale $t_{rh} \sim 8$ Gyr (Djorgovski and Meylan, 1993).

2.1 Method

The main aim of our study is to analyze the photometry and kynematics of the cluster. In order to have a complete census of the stars both in the internal dense regions and in the external parts, this work will be based on two catalogs: HST UV Globular Cluster Survey (HUGS, Nardiello et al., 2018) and Stetson et al. (2019) catalog. Both of them have to be cross-matched with catalogs that give information about the kinematics of the stars, like proper motion. HST is implemented with Hubble Space Telescope Atlases of Cluster Kinematics (HACKS, Libralato et al., 2022), while Stetson with GAIA DR3 dataset (Gaia Collaboration, 2023). For both the two combined catalogs, the study goes trough multiple data rejection, based on astrometric, photometric and dynamical characteristics of the stars. This passages remove stars that do not belong to the cluster (field stars) and leave to us only cluster stars that share the same values in term of proper motions and photometric parameters. At the end is possible to study in deep the two populations in the cluster by looking at their distributions and compare with other clusters in the literature.

2.2 HST catalog

HST offers very high precision and accuracy when the aim of the study is multiple populations in GCs, especially in the innermost high-populated regions, where it's difficult to disentangle single stars (Bastian and Lardo, 2018). HUGS catalog is based on imaging clusters through UV/blue WFC3/UVIS filters F275W, F336W, and F438W, which complement the existing F606W and F814W database. The first three filters has shown particular abilities to characterize MP patterns in GCs, due to their high level of sensitivity to C, N, and O abundance variations (Piotto et al., 2015). This photometric database has to be implemented with data about internal kinematic of the cluster, hence by adding to HUGS catalog proper motions of each star. We did this by using HACKS data. In order to obtain a complete dataset of stars in HUGS catalog with their proper motions, the first tool we used is `CataXcorr`, which does cross-match the stars in HUGS and HACKS fields. The final dataset is HUGS catalog but with Right ascension (Ra) and Declination (Dec) in HACKS frame. The final tool that produces the dataset to be used in the study is `Catacomb`, which associate each proper motion to the right star in HUGS field. Now, with a complete dataset in terms of photometry and kinematics, we proceeded by producing the Color-Magnitude Diagram (CMD) of NGC 5053 in three different colors (**Figure 2.1**).

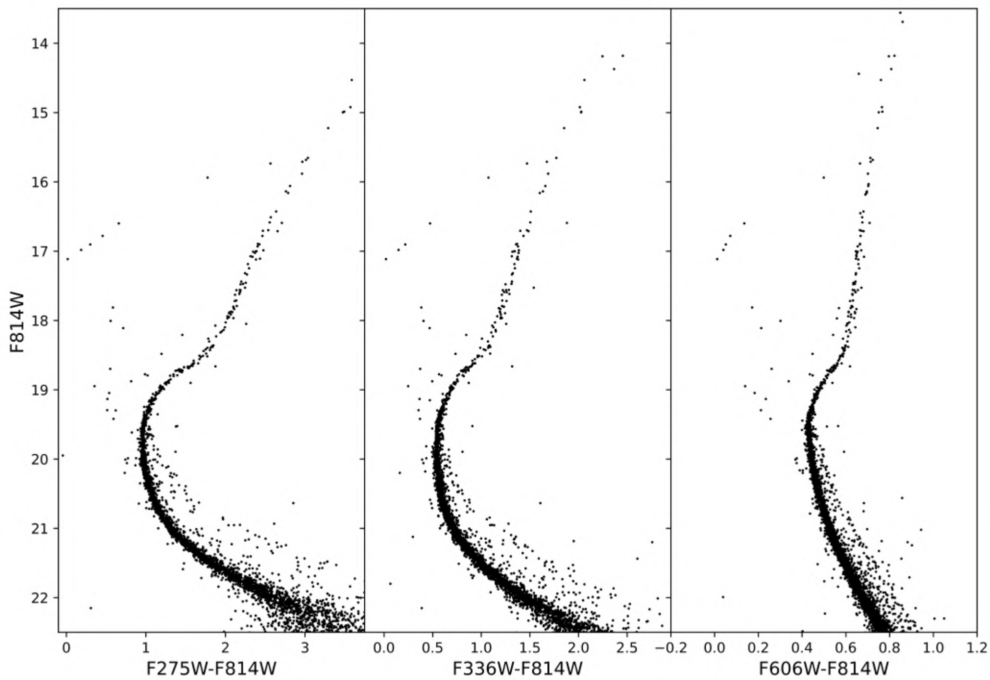

Figure 2.1: CMD in three different colors of NGC 5053, considering stars within 100 arcsec from the cluster center.

In all of them the Main Sequence (MS) and the Turn Off (TO) is well defined, as for Red Giant Branch (RGB). At fainter magnitudes the MS is more scattered since photometric measurements tend to be less accurate.

The first relevant problem here is that these CMDs are contaminated by field stars. Since it is not possible to rely on photometry, a good method to reject field stars is by studying proper motions. Stars that belong to GC have proper motion values, both in Ra and Dec direction, which are scattered inside a defined region around the mean values of the cluster, while field stars show different proper motion values. By considering CMD in F606W-F814W color, we divided it in 5 magnitude bins and for each of them we produced a Vector-Point Diagram (VPD) of relative proper motions (**Figure 2.2**). A circle around the cluster centroid in VPD defines our membership criterion. The chosen radius is a compromise between losing cluster members with poor proper motions and including field stars that share the cluster mean proper motion. Since HST has a high resolution but a small Field of View, the field contamination is not prominent, and affects CMD mostly at faint magnitudes. For each magnitude bin, the stars which belongs to NGC 5053 are constrained inside the red circle representing the 3σ selection.

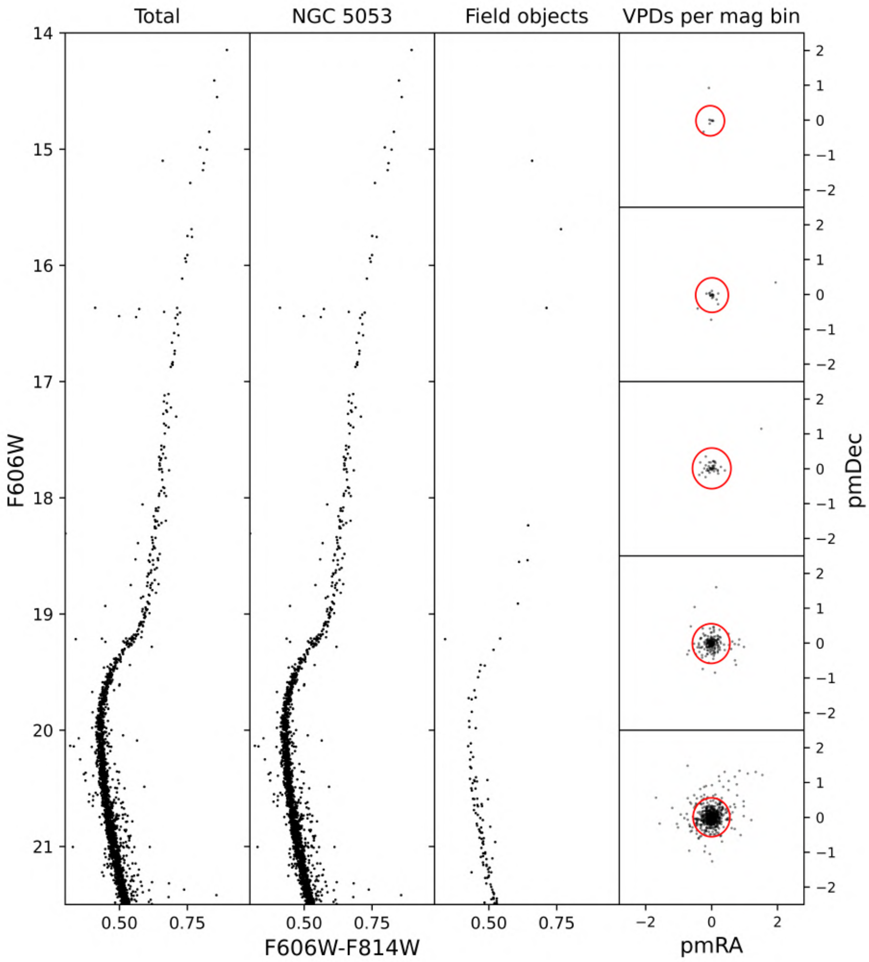

Figure 2.2: VPDs of relative proper motions for different magnitude bins. Field objects in the right CMD will be removed from our sample.

The further step involves magnitude errors which can be used to reject stars with errors that overcome 3σ level. Each magnitude dataset is divided into bins, and for each bin a mean magnitude error is derived. Stars with magnitude errors that exceed 3σ in each bin are rejected. From **Figure 2.3** it is clear that this selection must be done by considering different mean magnitude errors, since their distribution become less scattered while reaching brighter magnitudes. The red points are the stars rejected by the selection. CMDs in (**Figure 2.4**) shows the result of this photometric selection. In the right-hand panel we used a special photometric color index, C_{UBI}, which separates stars based on their chemical properties, namely N and He abundances (Monelli et al., 2013). In HST photometry, C_{UBI}=(F275W-F346W)-(F346W-F438W).

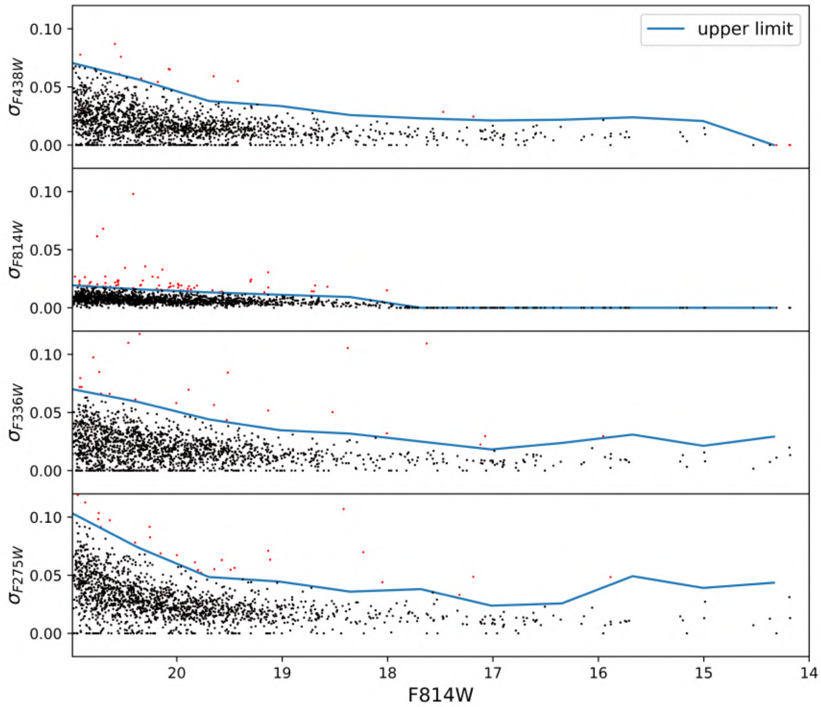

Figure 2.3: Magnitude errors for all the magnitudes. The blue line gives the 3σ upper limit.

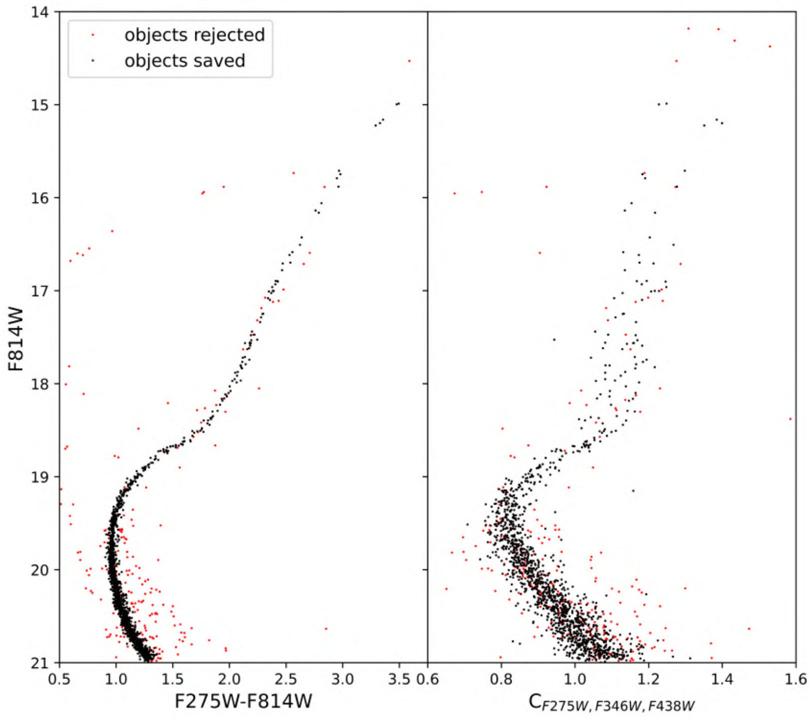

Figure 2.4: CMDs of NGC 5053 with rejected stars (in red) based on Figure 2.3. The right-hand panel shows CMD in C_{UBI} color index.

2.2.1 Selection of Multiple Populations

Thanks to photometric and kinematic selections, we were able to study the presence of multiple stellar populations in this cluster, focusing on the photometric index C_{UBI}:

1. For each (equally sized) magnitude bin covering RGB in C_{UBI} diagram, we derived points of 4th and 96th percentiles;

2. We fitted them with a 1D polynomial (Milone et al., 2017) obtaining two fiducial ridgelines;

3. We normalized the C_{UBI} distribution:

$$\Delta C_{\mathrm{UBI}} = \frac{C_{\mathrm{UBI}} - X_{\mathrm{blue}}[\mathrm{F814W}]}{X_{\mathrm{red}}[\mathrm{F814W}] - X_{\mathrm{blue}}[\mathrm{F814W}]} - 1. \tag{2.1}$$

   X_{red} and X_{blue} are red and blue fiducial ridgelines in the left-hand panel of **Figure 2.5**. The resulting ΔC_{UBI} distribution is shown in the top-right panel;

4. We plotted a histogram in the bottom-right panel, representing ΔC_{UBI} distribuition.

The histogram shows two distinguished peaks in correspondence of the two fiducial ridgelines: this points out the presence of two distinct populations in NGC 5053.

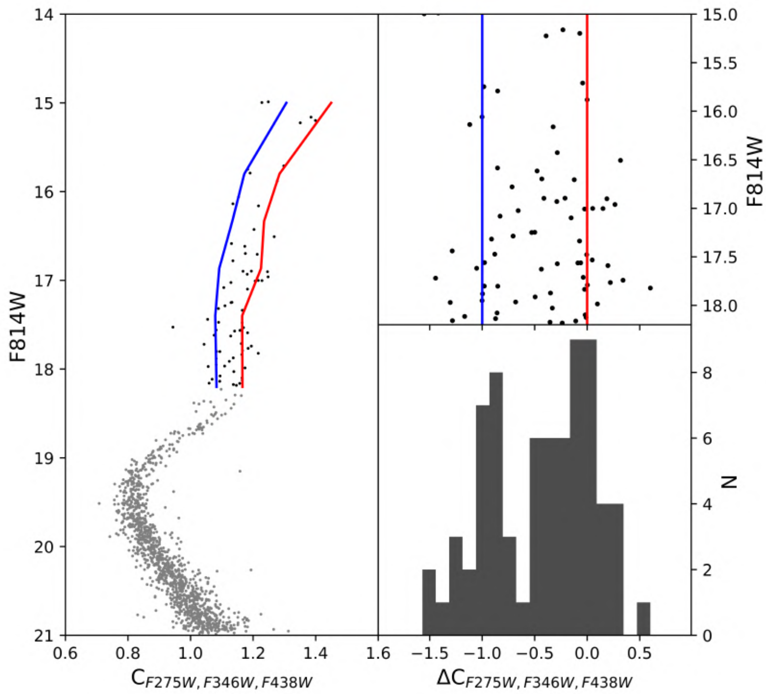

Figure 2.5: Left-hand panel: The C_{UBI} distribution of NGC 5053 stars in black on RGB, with the 4th percentile ridgeline in blue and the 96th percentile ridgeline in red. Right-hand panel: On top the resulting distribution ΔC_{UBI} of the same stars after normalization as described by equation (2.1). On bottom the distribution ΔC_{UBI} in terms of number of stars.

We did the same type of analysis by using (F275W-F814W) color index, which is sensible to He variations in stars, and so the corresponded $\Delta(F275W - F814W)$ (**Figure 2.6**). The two panels on the right show that this color index does not highlight the separation of two stellar populations. Instead, the histogram presents a unique peak between the fiducial ridgelines.

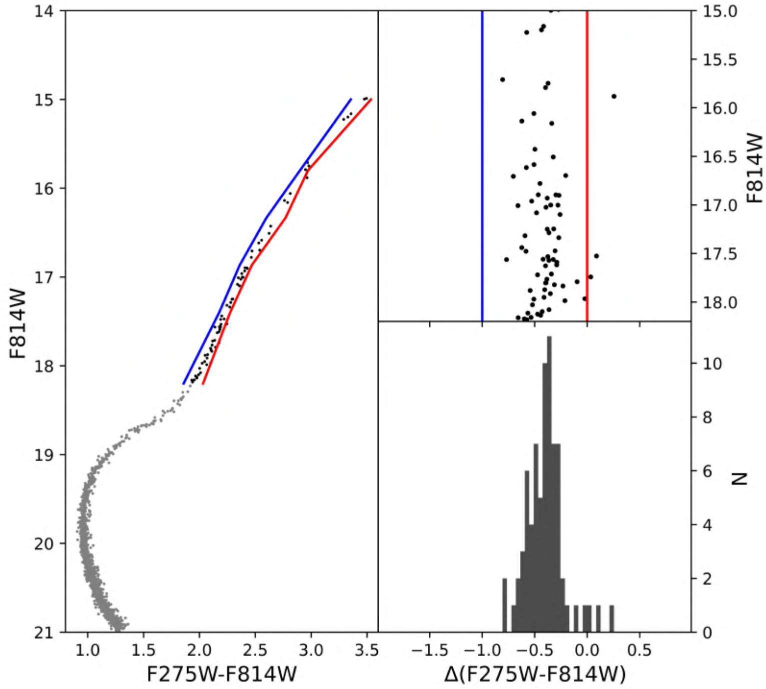

Figure 2.6: Left-hand panel: The (F275W-F814W) distribution of NGC 5053 stars in black on RGB, with the 4th percentile ridgeline in blue and the 96th percentile ridgeline in red. Right-hand panel: On top the resulting distribution $\Delta(F275W - F814W)$ of the same stars after normalization. On bottom the distribution $\Delta(F275W - F814W)$ in terms of number of stars.

In addition to the $C_{\rm UBI}$ colour distribution classification, it is also possible to separate populations using chromosome maps (Milone et al., 2017). A chromosome map is a colour–colour plot that allows efficient separation of sub-populations of different abundances. It uses the RGB stars distribution in **Figure 2.6**, along with the RGB distribution of $\Delta C_{\rm UBI}$ (**Figure 2.5**). In these instances, the two populations tend to be easier to distinguish using a chromosome map, as they can blend together when using the $\Delta C_{\rm UBI}$ distribution alone. We applied Gaussian Mixture Models (GMMs) (Pedregosa et al., 2011) in order to separate the two populations. The method uses an expectation–maximization approach to determine the best mixture of one or more Gaussians to fit the $\Delta C_{\rm UBI}$ and $\Delta(F275W - F814W)$ distribution. By creating a chromosome map, we used the GMM method in two dimensions (**Figure 2.7**), in order to highlight the two populations with two ellipses.

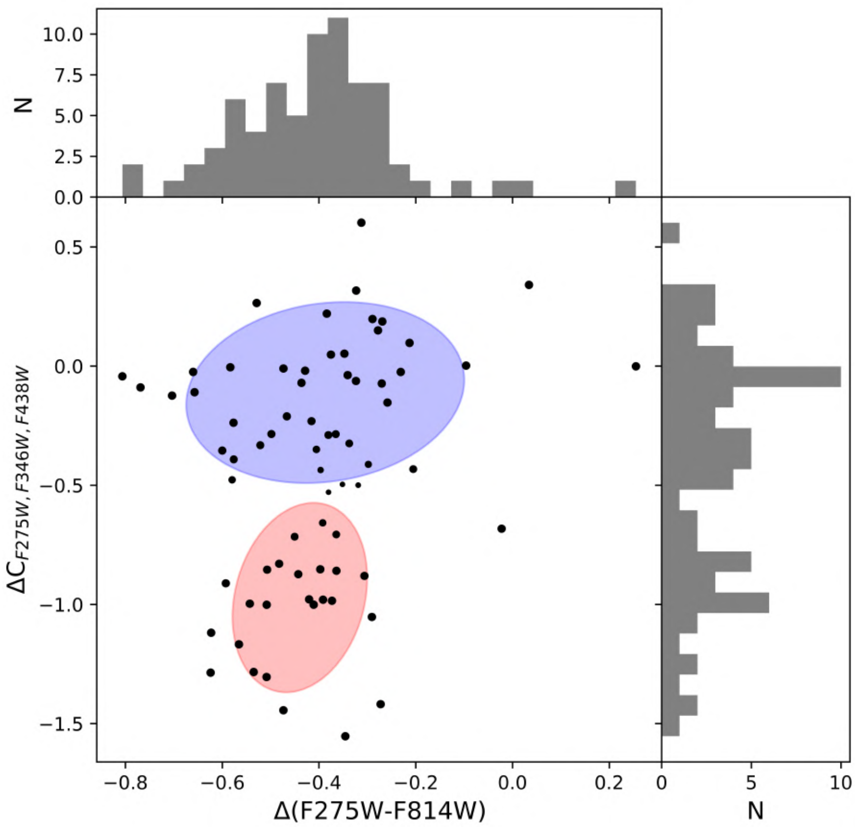

Figure 2.7: Chromosome map using the HST photometry for NGC 5053, with Gaussian Mixture Models (GMMs) applied in two dimensions. The lower left plot shows the chromosome map with populations P1 (red) and P2 (blue) as defined by the two distributions in the top and right-hand panels.

In this chromosome map, the x-axis is mainly sensitive to variations in He while the y-axis is dominated by variations in N (at C, O to a lesser extent). Based on Milone et al. (2017), stars in population P2 have peculiar chemical composition as enriched or SG (second generation). On the contrary, stars in population P1 have field-like abundances as primordial or FG (first generation). This separation led us to the creation of two distinct datasets, one for each population, where stars with a probability $> 50\%$ to belong to FG are separated from stars with a probability $> 50\%$ to belong to SG. At the end we obtained 78 stars divided in 27 FG and 51 SG.

2.3 Stetson et al. catalog

Stetson et al. (2019) catalog present wide-field, ground-based Johnson–Cousins UBVRI photometry for 48 Galactic globular clusters. These data provide a bridge between existing small-area, high-precision HST photometry and all sky catalogs from large surveys like Gaia, SDSS, or LSST. For NGC 5053, it provides the photometry of over 30000 objects spanned in a region of 2500x2500 arcsec. **Figure 2.8** clearly shows that only a fraction of these objects belongs to the cluster, which is identified by three radii:

- core radius (R_{C}) is the radius for which the value of the density is equal to half the central density;
- half-light radius (R_{HL}) is the radius from within which half of the total cluster mass is contained;
- truncation radius (R_{T}) is the radius at which gravitational potential of the MW cannot be neglected anymore and the stars no longer belong to the cluster.

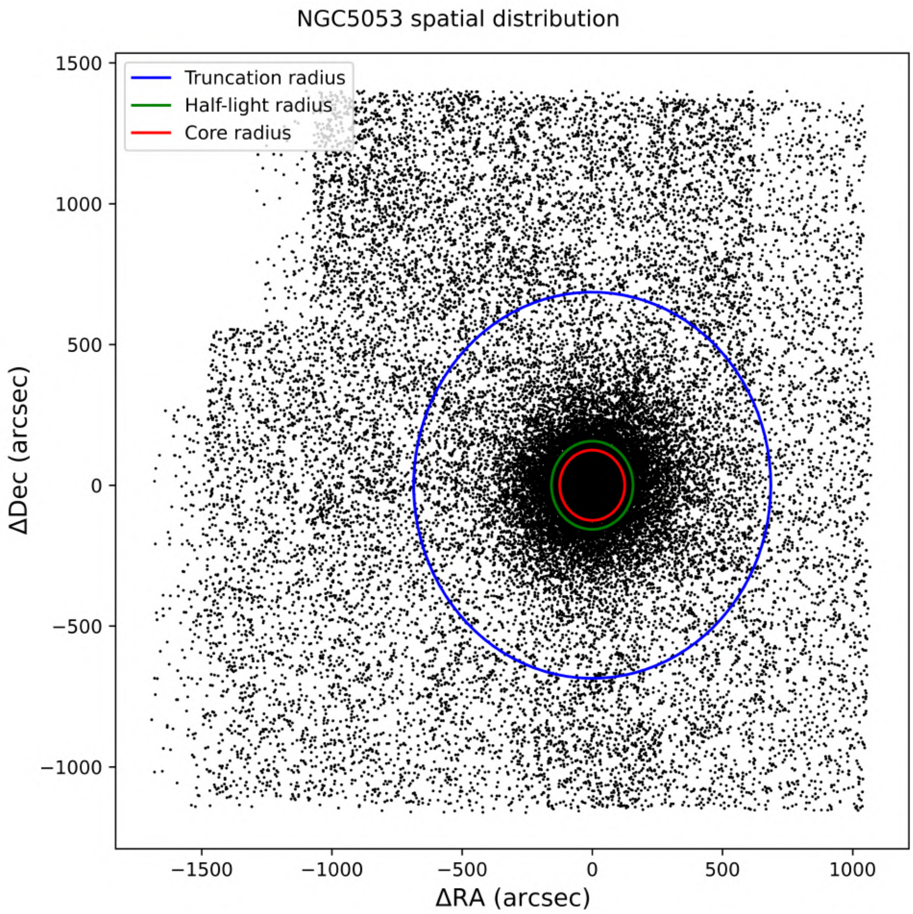

Figure 2.8: Spatial distribution of NGC 5053 using Stetson. The cluster is constrained by the 3 circles related to R_{C}, R_{HL} and R_{T}.

From Baumgardt et al. (2023) we took $R_{\mathrm{C}} = 9.2$ pc, $R_{\mathrm{HL}} = 12.4$ pc and $R_{\mathrm{T}} = 91.64$ pc.

The steps followed in part 2.2 are applied also in this study case, with some differences due to the catalogs used. Stetson catalog needs to be implemented in order to have kynematic constraints like proper motions. We integrated our photometric catalog with GAIA DR3 dataset, which provides the absolute proper motions of stars along with several photometric and astrometric quality indicators. Using `CataXcorr` and `Catacomb`, we obtained a cross-matched catalog of over 34000 stars with Stetson photometry and with proper motions from Gaia data release. With this dataset we created CMD in three different colors using a combination of U,V, B and I filters (**Figure 2.9**).

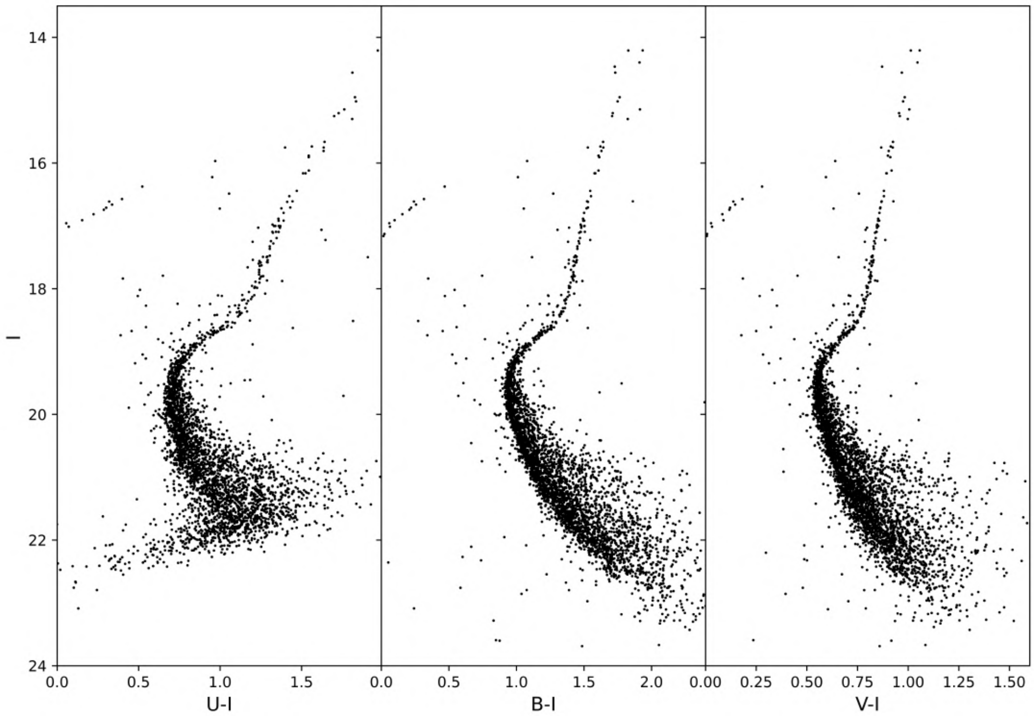

Figure 2.9: CMDs in three different UBVRI colors with stars within 100 arcsec from cluster center.

As for HST photometry, the color index is scattered for faint stars, especially in (U-I) versus I diagram. The RGB is poorly populated with respect to MS, especially at I magnitudes lower than 16.

We than focused on the rejection of objects that do not belong to the cluster in terms of kinematics, using proper motions as constraint. **Figure 2.10** shows (V-I) versus V diagram and VPDs of relative proper motions for each V magnitude bin. The rejection is effective at bright magnitudes, while at faint magnitudes the big uncertainties related to proper motions leave many objects outside the MS. This will not affect our analysis, since our focus for the study of multiple populations is on RGB, where the rejection worked well.

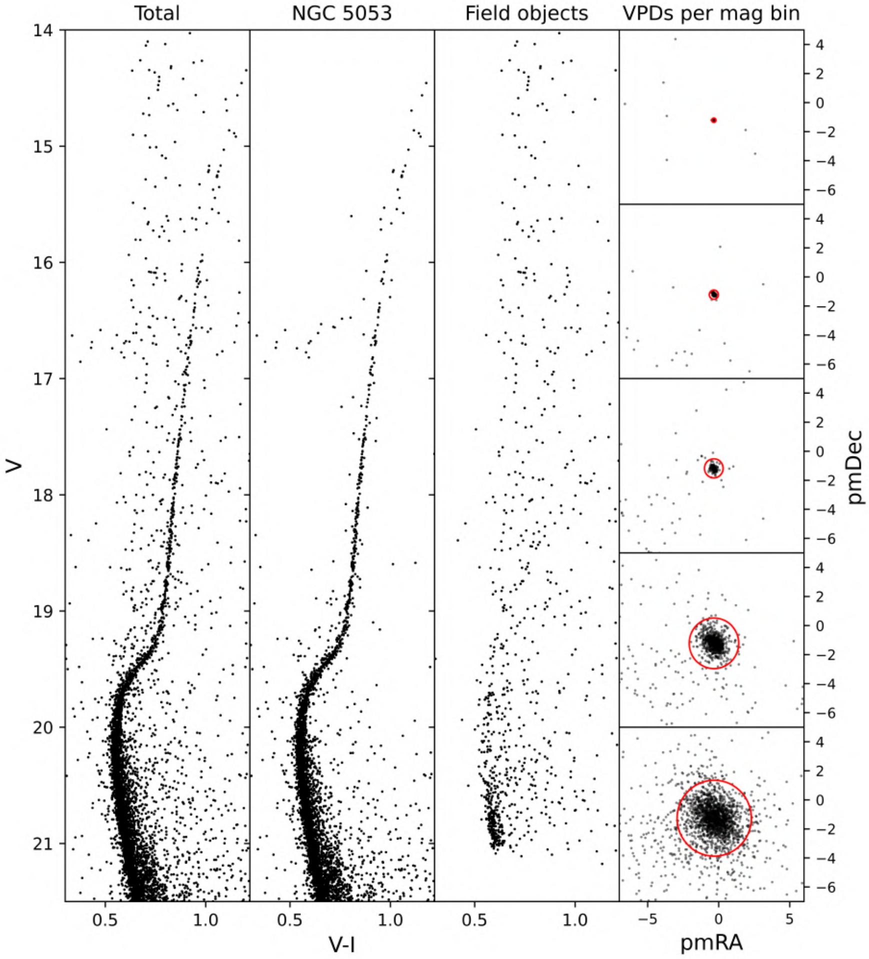

Figure 2.10: VPDs of relative proper motions for different V magnitude bins. Field objects in the right CMD will be removed from our sample.

With this new catalog we applied the rejection based on magnitude errors. We also used sharpness value, which gives an indication on how much a light source is similar to a point-like object. This constraint is useful in this study case since it is able to reject galaxies in the wide field. As for magnitude errors, also for sharpness the mean was derived for different magnitude bins. For each mean, we calculated 3σ error which gives an upper and lower limit for the rejection of the objects (**Figure 2.11**). Both magnitude errors and sharpness are less scattered at bright magnitudes, while most of the reject objects are the fainter ones, due to big uncertainties in the detection process. This step gave us a new refine catalog. (U-I) versus I diagram is shown in **Figure 2.12**, together with the one using special C_{UBI} = (U-B)-(B-I) color index. Red points are the rejected objects which will not be considered in the next steps.

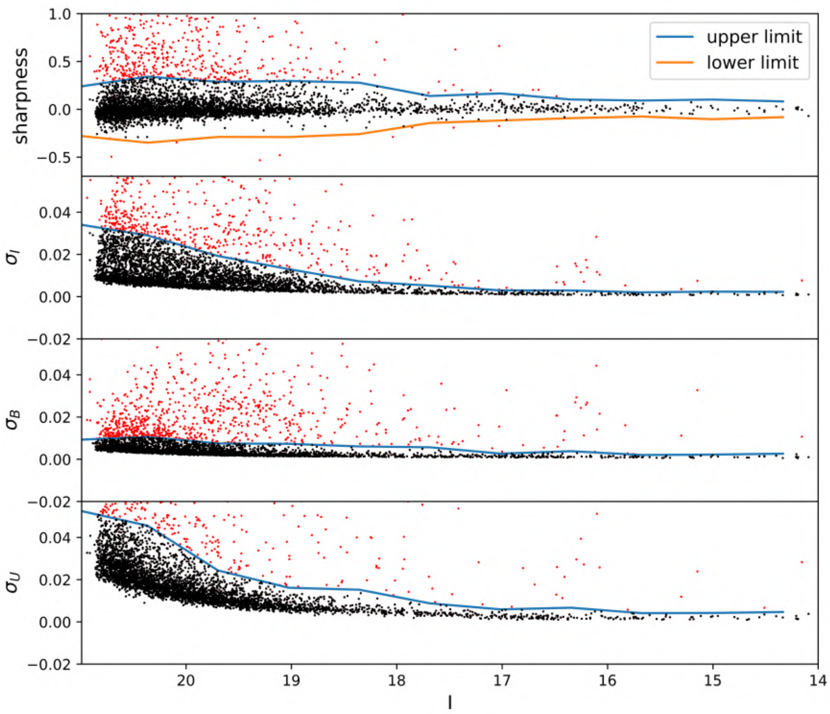

Figure 2.11: Magnitude errors in U,B and I filters. The upper panel shows the sharpness for each object. Blue line is the upper limit and the orange one is the lower limit for sharpness.

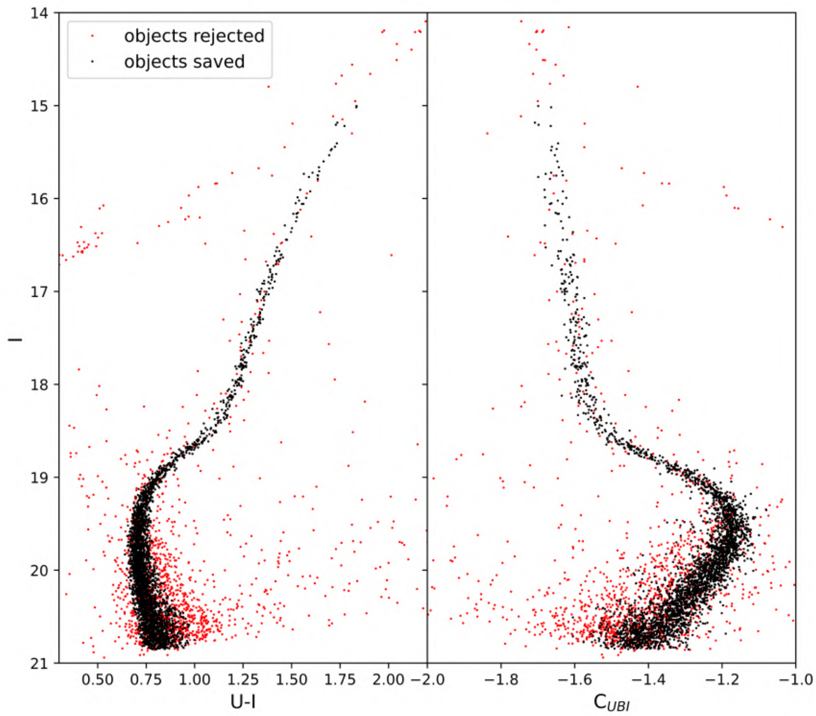

Figure 2.12: CMDs of NGC 5053 with rejected stars (in red) based on Figure 2.11. The right-hand panel shows CMD in C_{UBI} color index.

2.3.1 Selection of Multiple Populations

With this last rejection process we moved to the study of multiple populations. Color indices B-I and C_{UBI} are sensitive to variations in terms of chemical abundances within stars. In particular, (B-I) is sensitive to He while C_{UBI} to He and N variations. We derived ΔC_{UBI} and $\Delta(B-I)$ following equation 2.1, with X_{red} and X_{blue} ridgelines computed in I filter. ΔC_{UBI} is useful to constrain two distinct populations in RGB of **Figure 2.13**, especially by looking at the bimodal distribution in the bottom right-hand panel. On the contrary, $\Delta(B-I)$ in **Figure 2.14** does not give a solid indication on the presence of two separate populations, with a Gaussian distribution of stars between the two fiducial ridgelines.

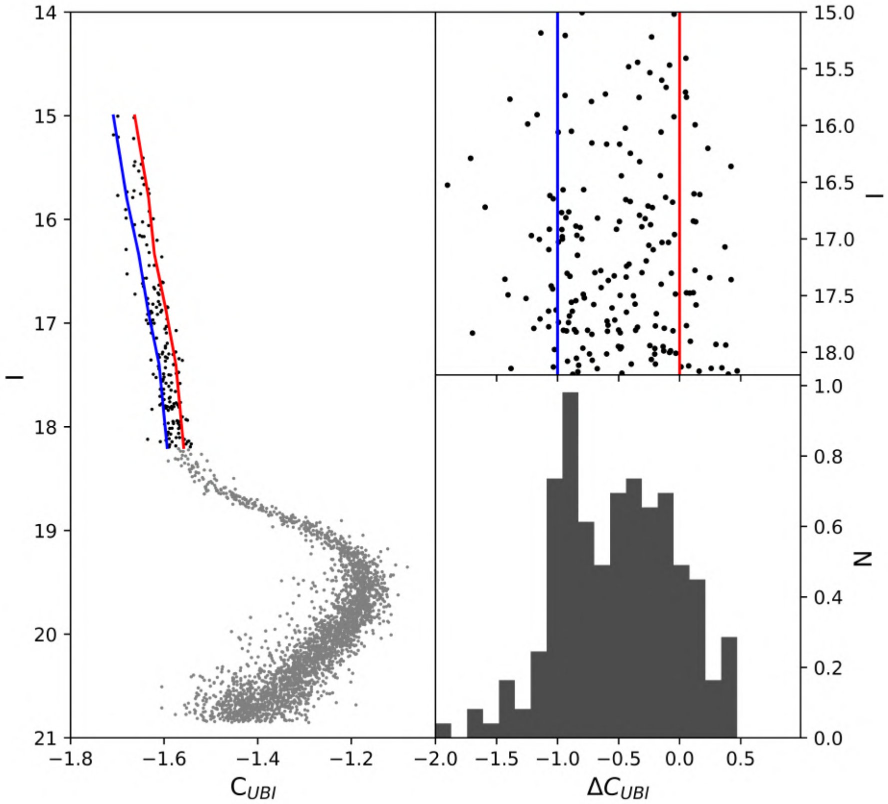

Figure 2.13: Left-hand panel: The C_{UBI} distribution of NGC 5053 stars in black on RGB, with the 4th percentile ridgeline in blue and the 96th percentile ridgeline in red. Right-hand panel: On top the resulting distribution ΔC_{UBI} of the same stars after normalization as described by equation (2.1). On bottom the distribution ΔC_{UBI} in terms of number of stars.

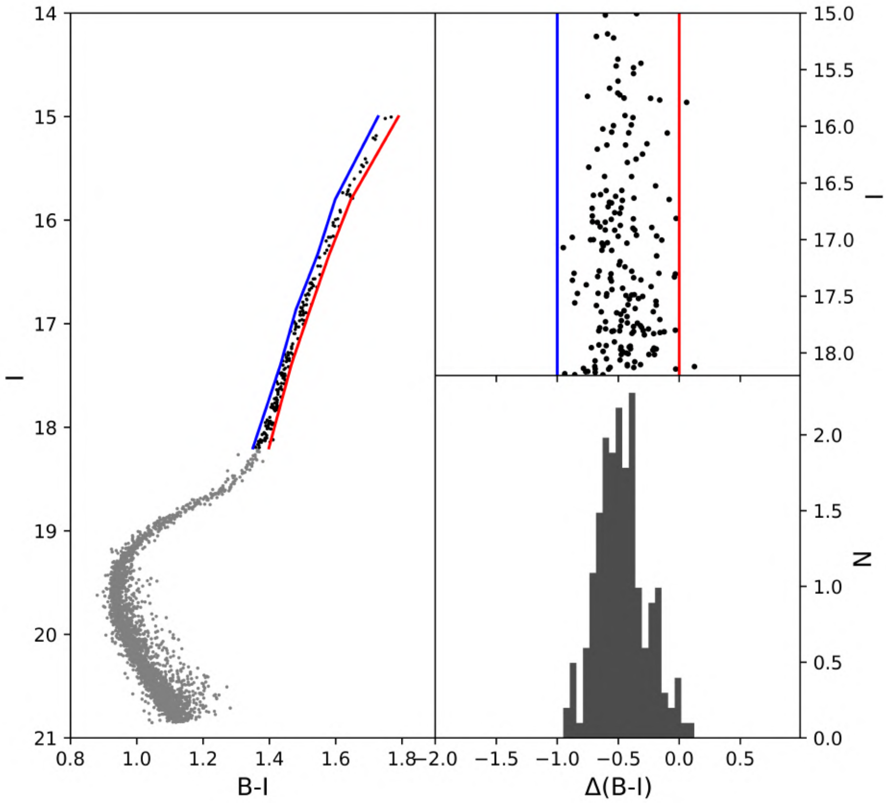

Figure 2.14: Left-hand panel: The (B-I) distribution of NGC 5053 stars in black on RGB, with the 4th percentile ridgeline in blue and the 96th percentile ridgeline in red. Right-hand panel: On top the resulting distribution $\Delta(B-I)$ of the same stars after normalization. On bottom the distribution $\Delta(B-I)$ in terms of number of stars.

To better distinguish the two populations, we created a chromosome map considering ΔC_{UBI} and $\Delta(B-I)$ distributions (**Figure 2.15**). We noticed that the FG stars (in red ellipse) and SG stars (in blue ellipse) are less separated between each other by comparing this chromosome map to the one in **Figure 2.7** using HST photometry. This can be related to the higher number of stars involved in Stetson catalog, both in FG and SG region. In addiction, the combination of filters used here is less effective than the one used with HST photometry. At the end we obtained 188 stars divided in 93 FG and 95 SG.

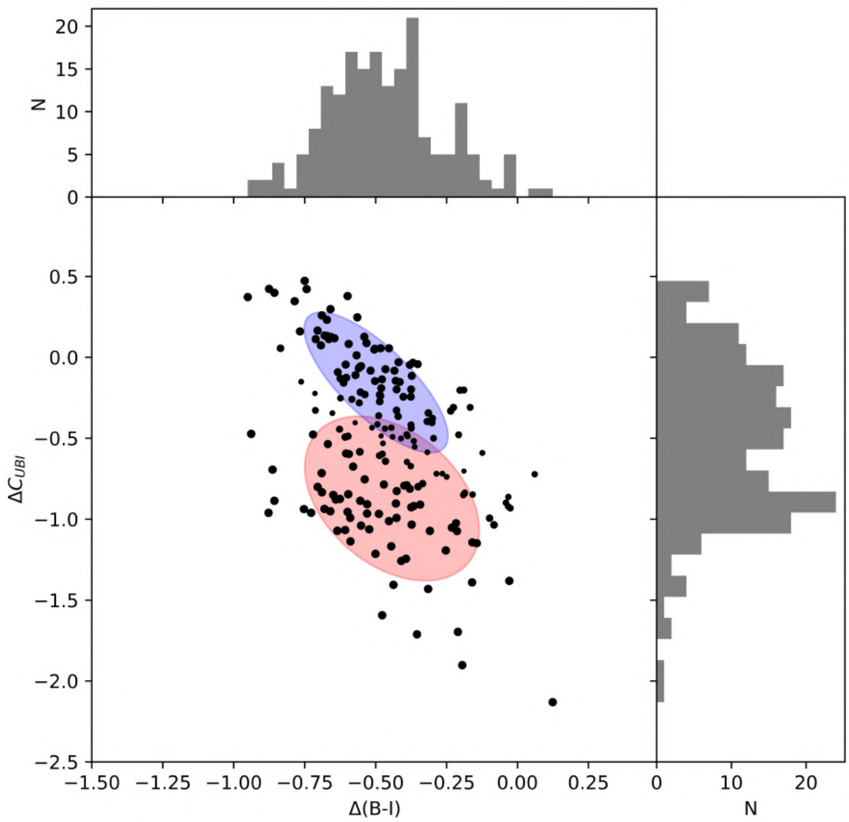

Figure 2.15: Chromosome map using Stetson for NGC 5053, with Gaussian Mixture Models (GMMs) applied in two dimensions. The lower left plot shows the chromosome map with populations P1 (red) and P2 (blue) as defined by the two distributions in the top and right-hand panels.

2.4 Results

In this section we combine together FG stars derived from HST and Stetson, and the same we do for SG stars. In this way, we can study the spatial distribution of the two populations using different tools, in order to have a better comprehension of the dynamics occurring in the cluster and its evolution history.
The first tool we used to study the behaviour of MPs as a function of radius is the cumulative radial distribution of the stars in each population. If one population is more centrally concentrated within the cluster, we see a steeper slope in its cumulative radial distribution with respect to the slope of the other one. However, if the populations are homogeneously mixed throughout the cluster, we see similar slopes for both distributions. The A^+ parameter (see equation (1.1)) is a way to quantify different radial profiles, as it is an integration of the "area" between the two distributions. Thanks to the combination between HST and Stetson photometry, we provide a spatially complete cumulative radial distributions, covering both inner and outer regions of the cluster. We calculated A^+ parameter as the difference between the areas below FG and SG cumulative radial dis-

tributions. The two areas were derived using jackknife resampling technique, giving an estimation of the two quantities with associated errors. **Figure 2.16** shows cumulative radial distributions of the two populations up to $2R_{\rm HL}$ and $R_{\rm T}$. A^+ parameter is also reported on each plot with the associated error, derived from the sum of squared errors related to FG and SG "areas". In the bottom panels we present the radial distribution of SG stars normalized to total. Within the first half of $2R_{\rm HL}$ neither FG nor SG dominates, while in the second half FG has a steeper cumulative distribution. The steepness of SG is quite constant along radius, hence the normalized number of SG stars stays costant around 60%. Focusing on the cumulative distribution up to $R_{\rm T}$, FG is more concentrated within 40% of the normalized radius, than its cumulative distribution becomes quite flat and it is overlapped by SG. Our A^+ parameter found within $R_{\rm T}$ ($A^+_{\rm T}$) is consistent with $A^+_{\rm total} = 0.07 \pm 0.16$ reported in Leitinger et al. (2023), confirming the steeper slope of FG with respect to SG. Overall, taken into account the errors, we can affirm that these two populations are dynamically mixed.

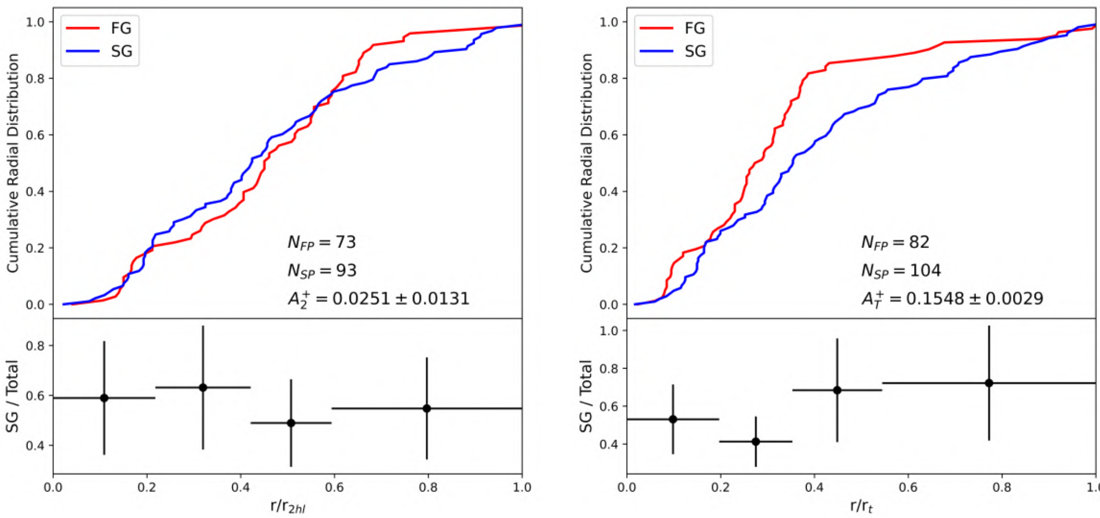

Figure 2.16: Top panels: Cumulative radial distribution of FG and SG stars up to $2R_{\rm HL}$ (upper plot) and $R_{\rm T}$ (lower plot). FG stars number($N_{\rm FP}$), SG stars number ($N_{\rm SP}$) and A^+ parameter are reported. Bottom panels: Radial distribution of SG stars over Total.

In order to better visualize the spatial distribution of MPs, we created 2-dimension plots centered in the center of NGC 5053. We highlighted FG and SG stars in two distinct panels (**Figure 2.17**), looking for relevant differences in their spatial distribution in inner and outer regions of the cluster.

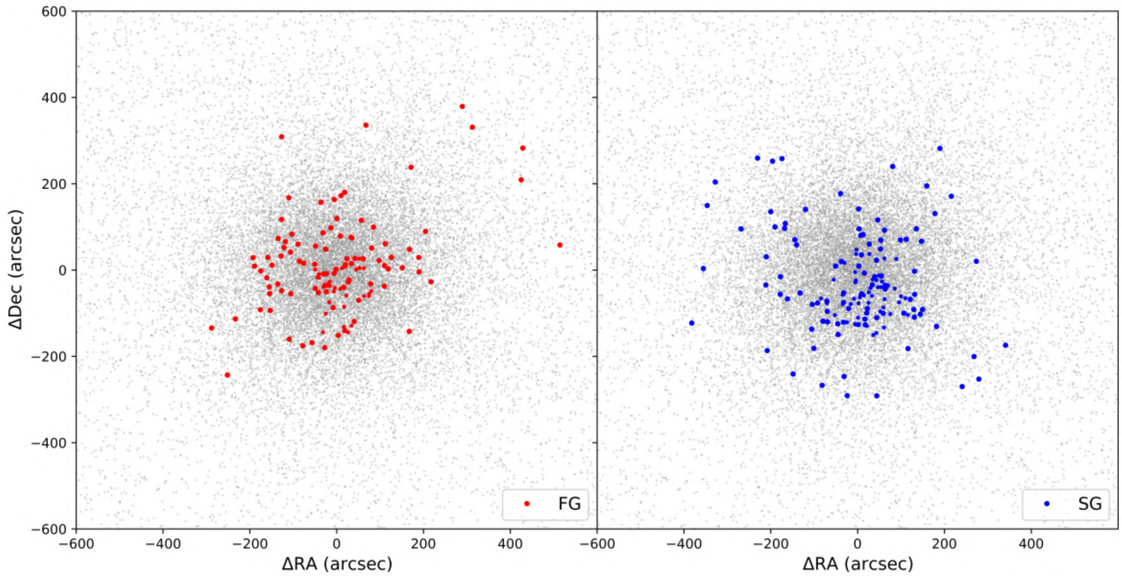

Figure 2.17: Spatial distribution of FG stars (left-hand panel, red dots) and SG stars(right-hand panel, blue dots) in NGC 5053.

The two distributions do not show significant differences. FG stars are equally distributed within 200 arcsec from the center, while SG shows a gap in the inner part of the cluster (due to low statistic) and presents few stars equally distributed above 200 arcesec. These results confirm that MPs in NGC 5053 are mixed together without a relevant separation. This is result is unattended, since NGC 5053 is a dynamically young GC.
We finally performed a 2-dimensional density map of the two populations for a better understanding of the distribution shape around the cluster center (**Figure 2.18**). To do this, we associated to each star a Gaussian distribution with specific bandwidth. In regions where stars are more concentrated, Gaussians sum up together, constraining a high-density region. We then added contour lines, which highlight the shape of these density regions around cluster center. While SG stars present a homogeneous radial density in the inner regions of the cluster, FG stars assume a more elliptical shape in their density distribution. These density maps can be compared with those of NGC 3201 created by Cadelano et al. (2024). While in NGC 3201 SG stars are more centrally concentrated than FG stars, in NGC 5053 the two populations share the same density distribution, confirming the mixing scenario. In the external regions, SG stars describe pretty asymmetrical and elongated distributions both in NGC 3021 and NGC 5053.

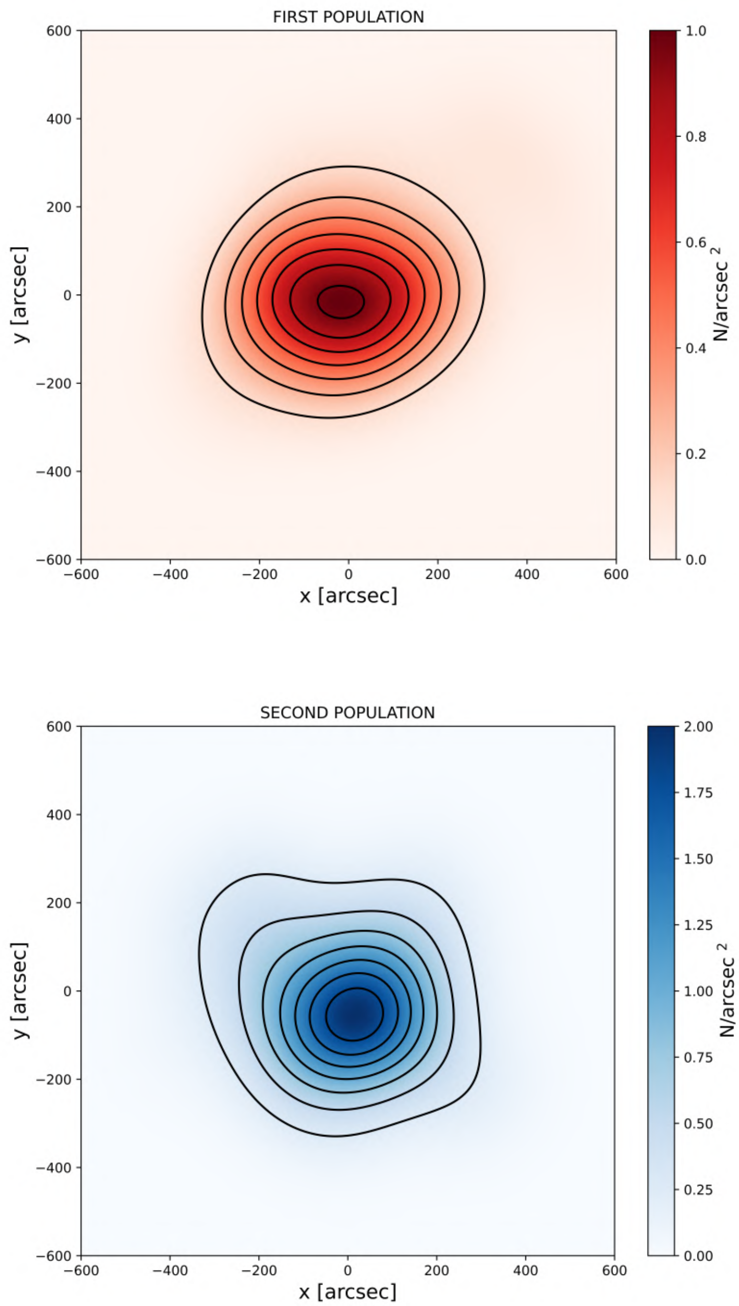

Figure 2.18: 2D density maps of FG stars (upper plot) and SG stars (lower plot) with contour lines in black. Density is color-coded by looking at the color bar on the right side of the two panels: dark color means high density region.

3 NGC 5466

NGC 5466 is a high galactic latitude GC (l = 42°.2, b = 73°.6), located in the constellation of Bootes at a distance of 16 kpc from the Sun (Harris, 1996). The cluster has been found to be surrounded by huge tidal tails (Belokurov et al., 2006). It presents a substantial population of blue stragglers stars (BSS), formed from the merger of the components of primordial, detached binaries that evolved into compact binary systems (Beccari et al., 2013). As NGC 5053, this is a metal poor cluster ([Fe/H]=−2.20), with a low mass M=5.6 · 10^4 $M_\odot$ and an exceptionally low stellar density ρ_c=7.9 $M_\odot/pc^3$ (Baumgardt et al., 2023). It is a dynamically young GC since $N_h=t/t_{rh}$=0.68, due to an estimated age t ∼ 13.57 Gyr (Marín-Franch et al., 2009) compensated by a half-mass relaxation timescale t_{rh} ∼ 19.9 Gyr (Beccari et al., 2013). We follow the steps presented in Chapter 2, focusing again on the photometric and kinematic analysis of the cluster to constrain MPs both in inner and outer regions.

3.1 HST catalog

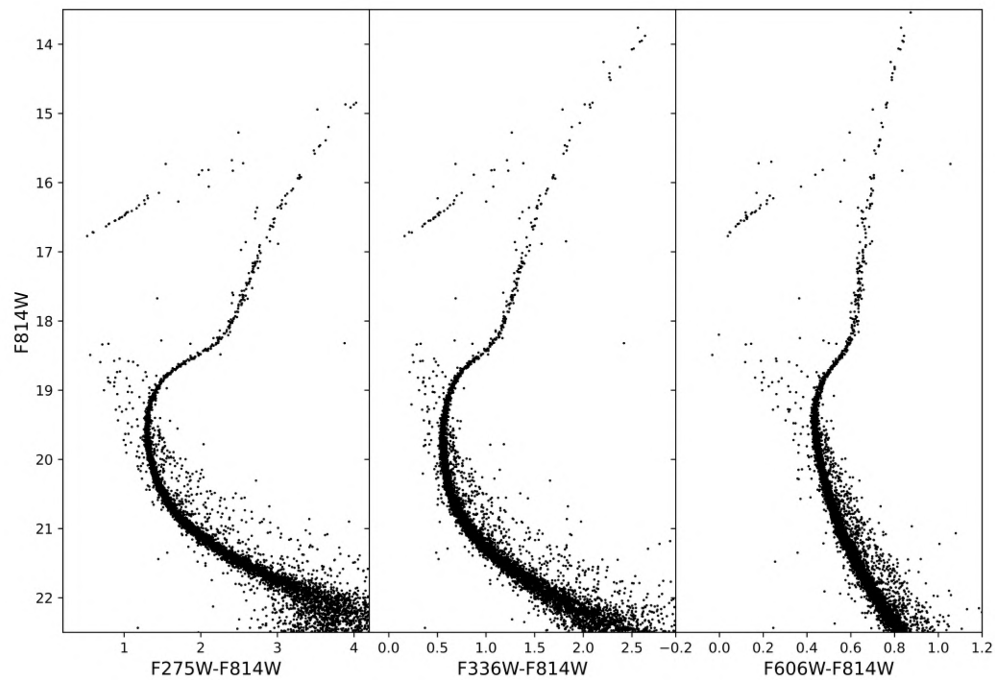

Figure 3.1: CMDs in three different colors of NGC 5466, considering stars within 100 arcsec from the cluster center.

Starting from HST photometry, we created a catalog of stars located in the inner regions of the cluster, with associated proper motions taken from HACKS. The CMDs in **Figure 3.1** show well defined MS and RGB, with scattered stars at faint magnitudes. Above the three TOs we notice the relevant presence of BSS.
Due to the low contamination in this catalog, the rejections associated to proper motions (**Figure 3.2**) and magnitude errors (**Figure 3.3**) seems not to be relevant, especially in the RGB. The rejection based on proper motions affected only few objects in MS, while the rejection based on magnitude errors removed only faint stars from the catalog.
Figure 3.4 shows the result of these selection steps, where the special color index in the right-hand panel is C_{UBI} (in HST photometry) and it will be used for the detection of MPs.

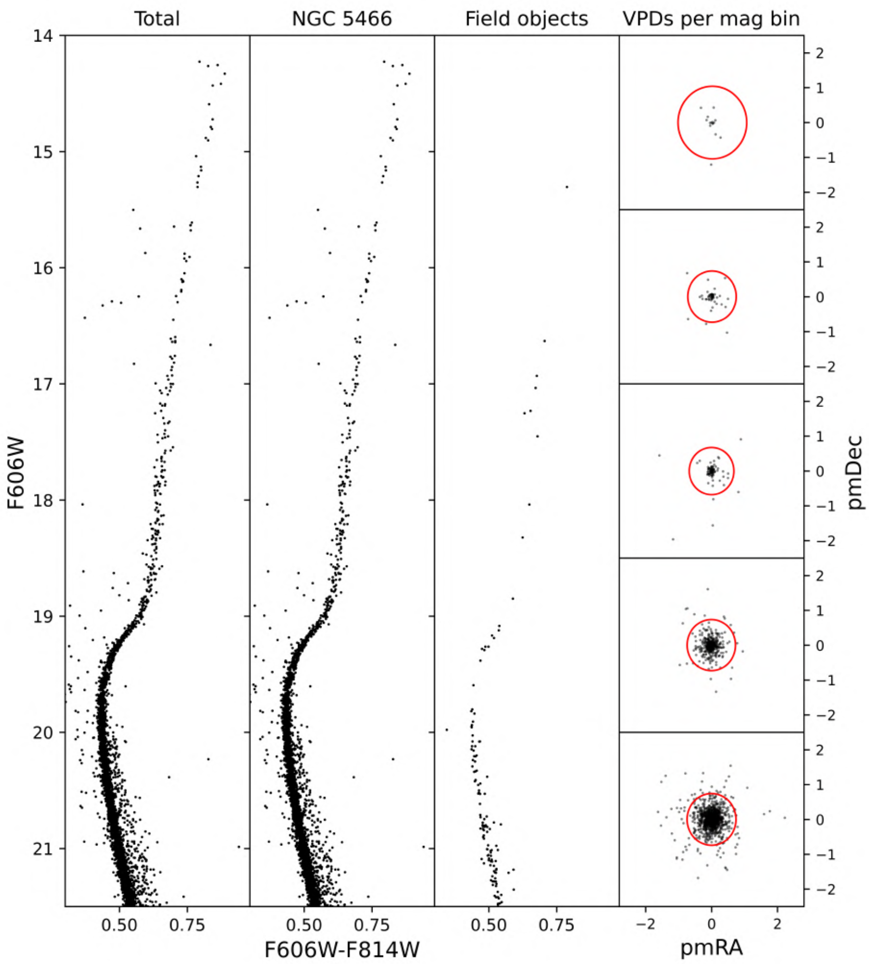

Figure 3.2: VPDs of relative proper motions for different magnitude bins. Field objects in the right CMD will be removed from our sample.

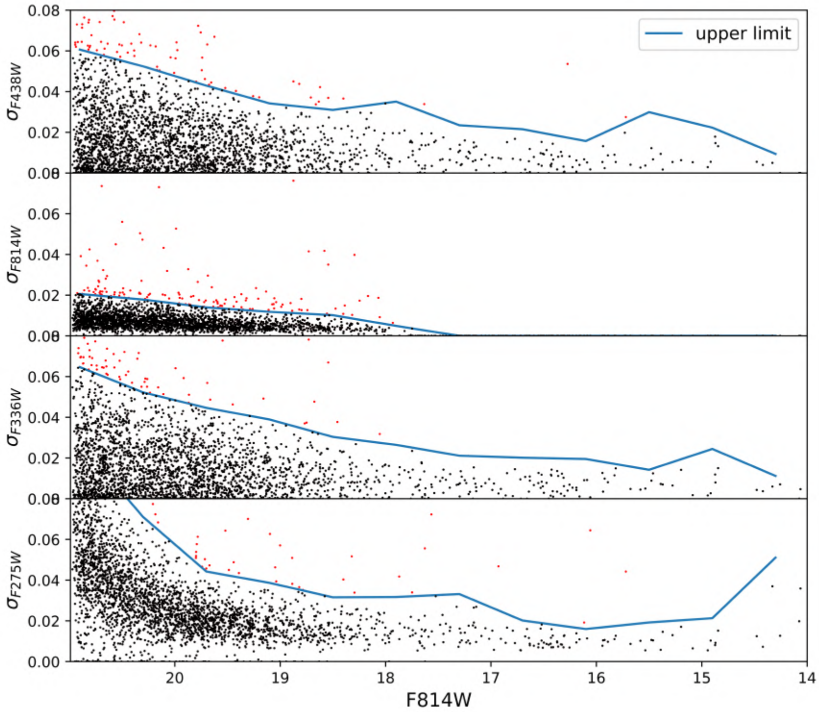

Figure 3.3: Magntiude errors for all the magnitudes. The blue line gives the 3σ upper limit.

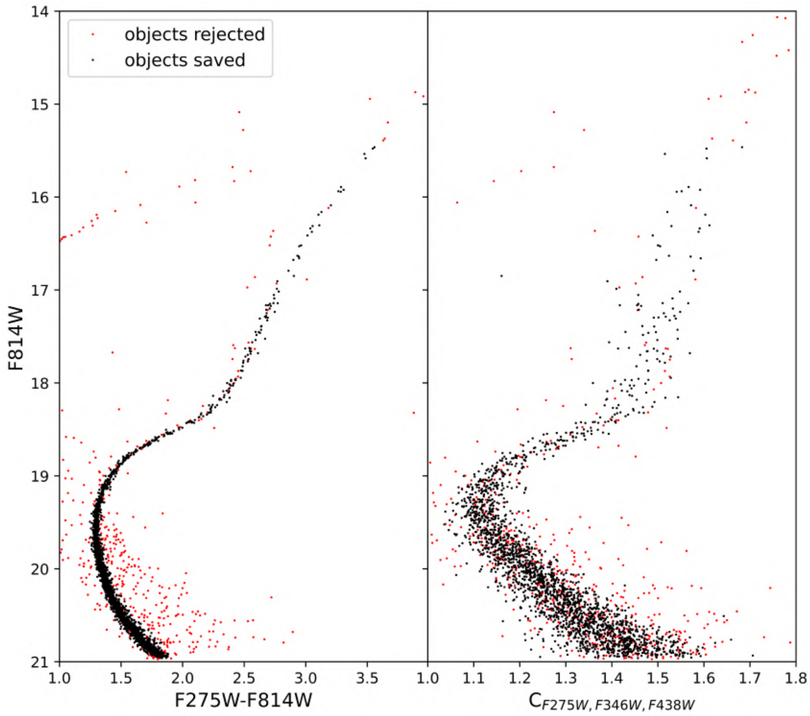

Figure 3.4: CMDs of NGC 5466 with rejected stars (in red) based on Figure 3.3. The right-hand panel shows CMD in C_{UBI} color index.

3.1.1 Selection of Multiple Populations

We proceeded with the analysis of MPs in NGC 5466, focusing on RGB. Using equation 2.1 we derived the normalized distribution of C_{UBI}, starting from 4th and 96th percentile ridglines (**Figure 3.5**). The right-hand panels show a bimodal ΔC_{UBI} distribution, expecially at magnitues brighter than 17. The first peak is split in two and shifted to the right with respect to the 4th percentile ridgline. We also produced the same plot using (F275W-F814W), where the separation of MPs is absent and so Δ (F275W-F814W) presents only one prominent peak between the two ridgelines (**Figure 3.6**).

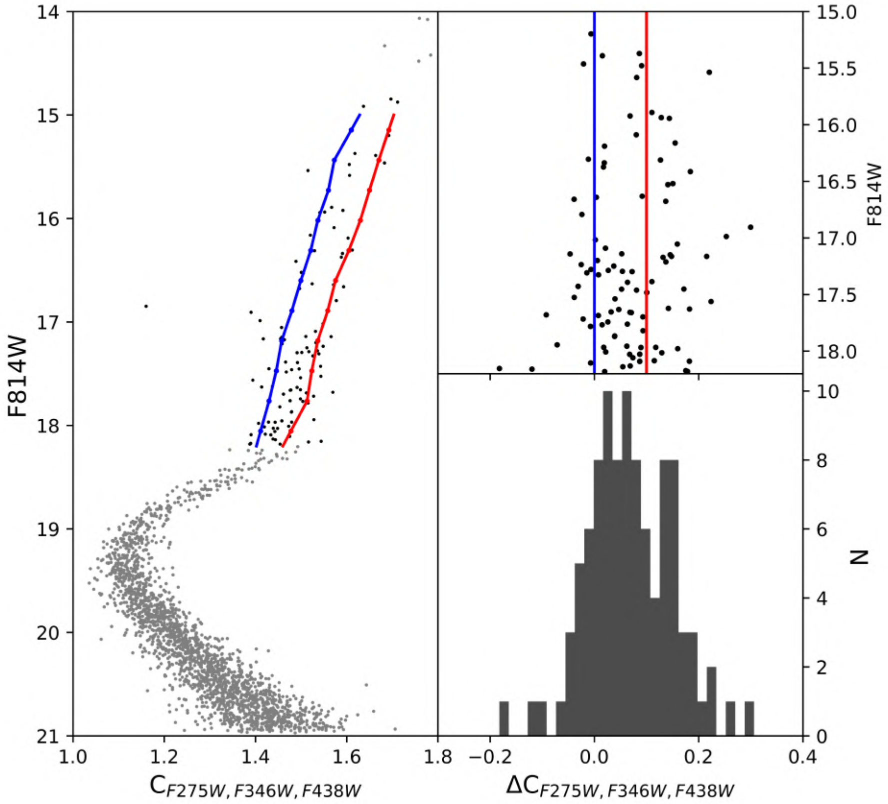

Figure 3.5: Left-hand panel: The C_{UBI} distribution of NGC 5466 stars in black on RGB, with the 4th percentile ridgeline in blue and the 96th percentile ridgeline in red. Right-hand panel: On top the resulting distribution ΔC_{UBI} of the same stars after normalization as described by equation (2.1). On bottom the distribution ΔC_{UBI} in terms of number of stars.

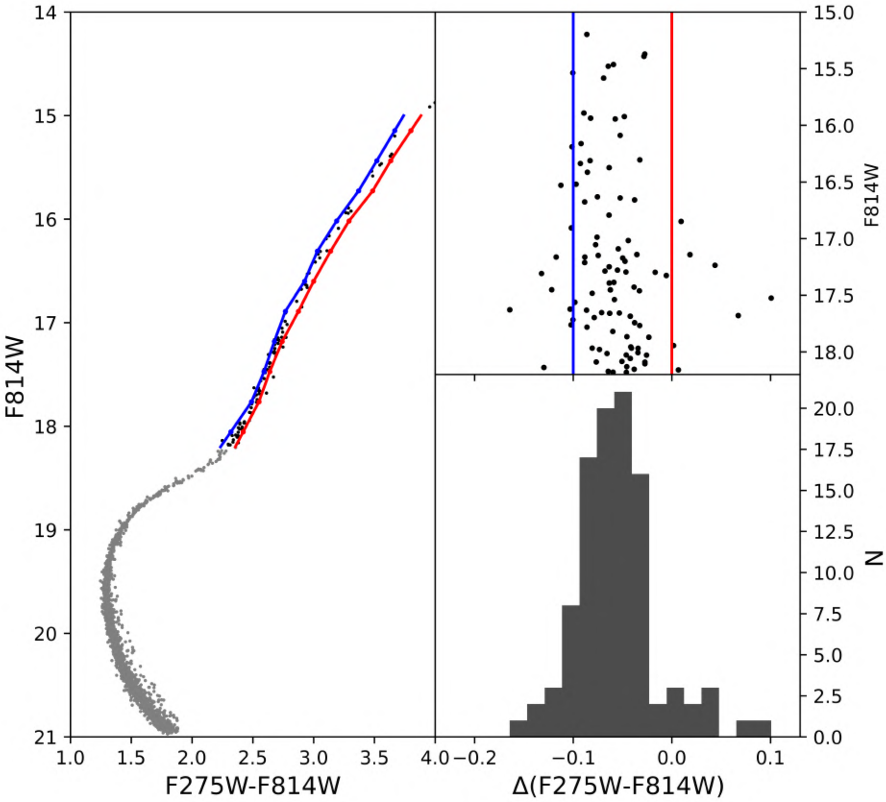

Figure 3.6: Left-hand panel: The (F275W-F814W) distribution of NGC 5053 stars in black on RGB, with the 4th percentile ridgeline in blue and the 96th percentile ridgeline in red. Right-hand panel: On top the resulting distribution $\Delta(F275W - F814W)$ of the same stars after normalization. On bottom the distribution $\Delta(F275W - F814W)$ in terms of number of stars.

Following the same method used with NGC 5053, we created chromosome map that enhances the separation of two populations, using the previous Δ(F275W-F814W) and $\Delta C_{\rm UBI}$ on x and y axis respectively. **Figure 3.7** shows FG stars in the red ellipse spanned in a constant range of $\Delta C_{\rm UBI}$ with the increasing of Δ(F275W-F814W). On the contrary, SG stars increase in y while x decreases, hence the enriched population in NGC 5466 suggests a strong He-N correlation (Bastian and Lardo, 2018). At the end we obtained 52 FG stars and 32 SG stars.

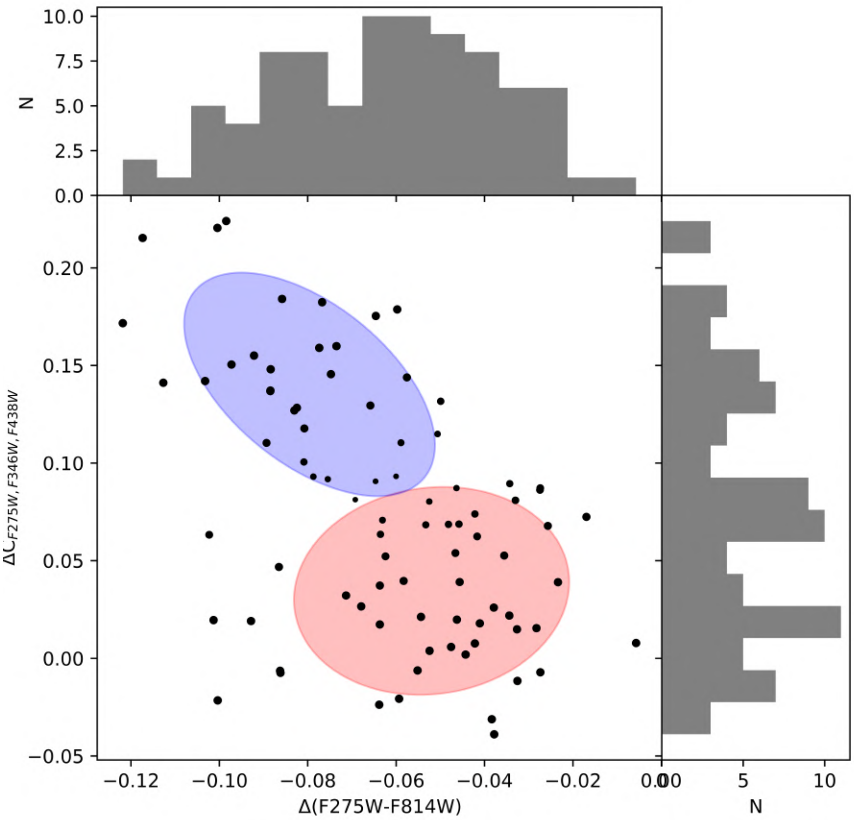

Figure 3.7: Chromosome map using the HST photometry for NGC 5466, with Gaussian Mixture Models (GMMs) applied in two dimensions. The lower left plot shows the chromosome map with populations P1 (red) and P2 (blue) as defined by the two distributions in the top and right-hand panels.

3.2 Stetson et al. catalog

Stetson catalog, implemented with Gaia kinematic data, presents more than 28000 objects for NGC 5466. CMDs in **Figure 3.8** show a well defined MS and RGB. Focusing on (V-I) diagram, we performed the first selection based on proper motions using VPDs (**Figure 3.9**). At bright magnitudes most of the field objects are rejected and we left with a clean RGB, while MS stars fainter than 21 are lost due to their scattered proper motions.

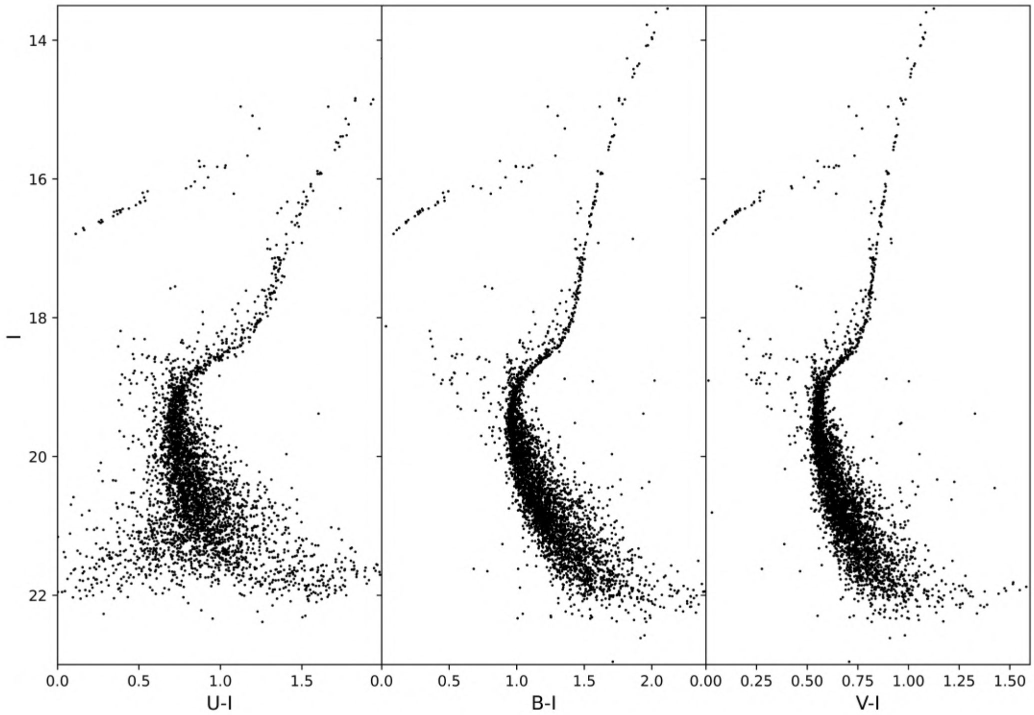

Figure 3.8: CMDs in three different UBVRI colors with stars within 100 arcsec from cluster center.

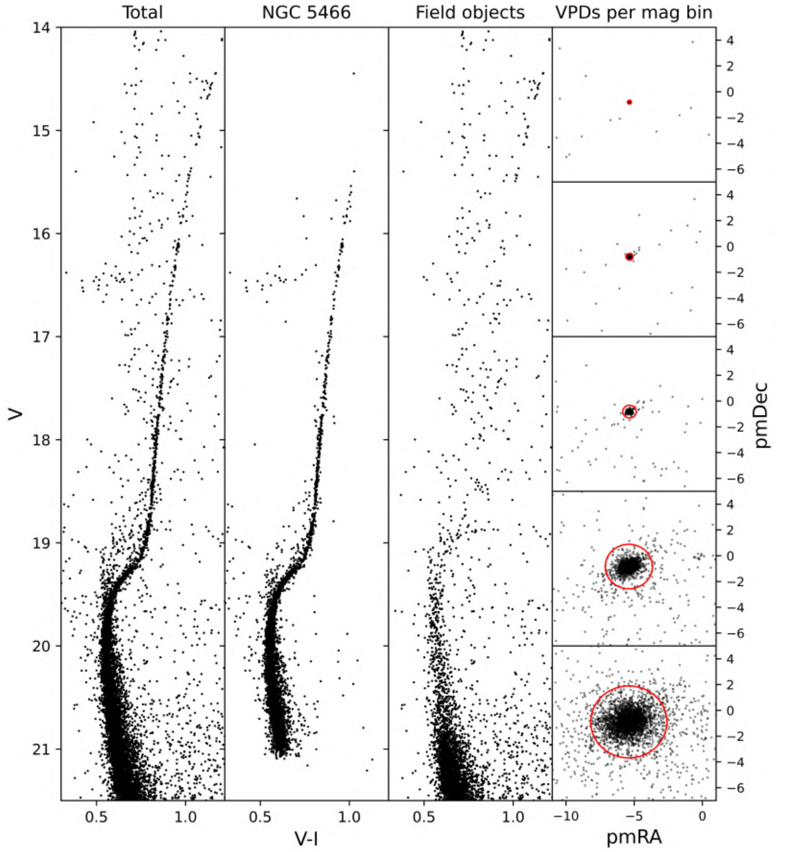

Figure 3.9: VPDs of relative proper motions for different V magnitude bins. Field objects in the right CMD will be removed from our sample.

With the resulting objects we moved to the rejection based on magnitude errors and sharpness value (**Figure 3.10**). Both magnitude errors and sharpness are less scattered at bright magnitudes, while most of the reject objects are the fainter ones, due to big uncertainties in the detection process. This step, implemented with MS+RGB box selection, gave us a new catalog. (U-I) versus I diagram is shown in **Figure 3.11**, together with C_{UBI} color index. Red points are the rejected objects which will not be considered in the next steps.

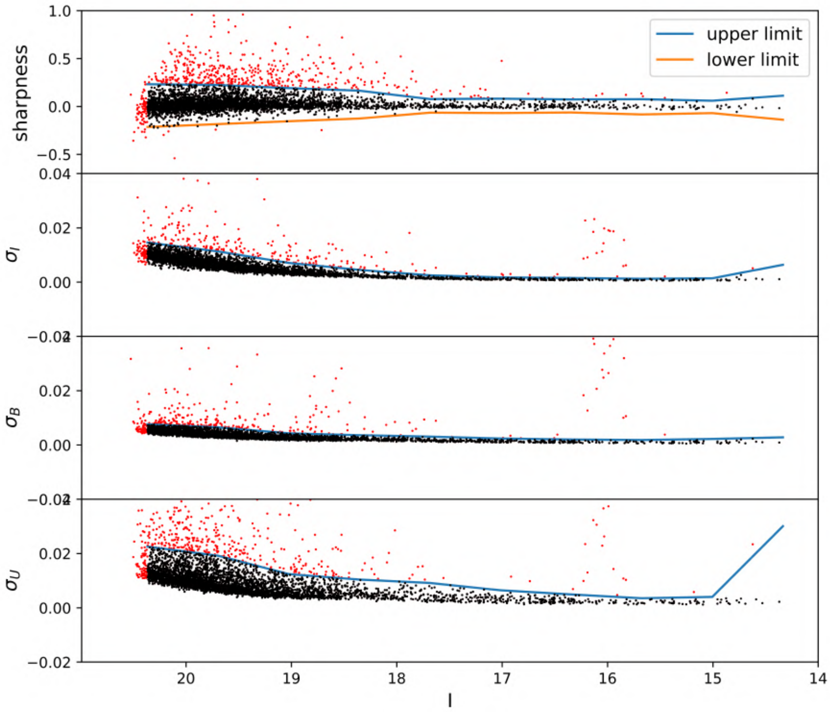

Figure 3.10: Magntiude errors in U,B and I filters. The upper panel shows the sharpness for each object. Blue line is the upper limit and the orange one is the lower limit for sharpness.

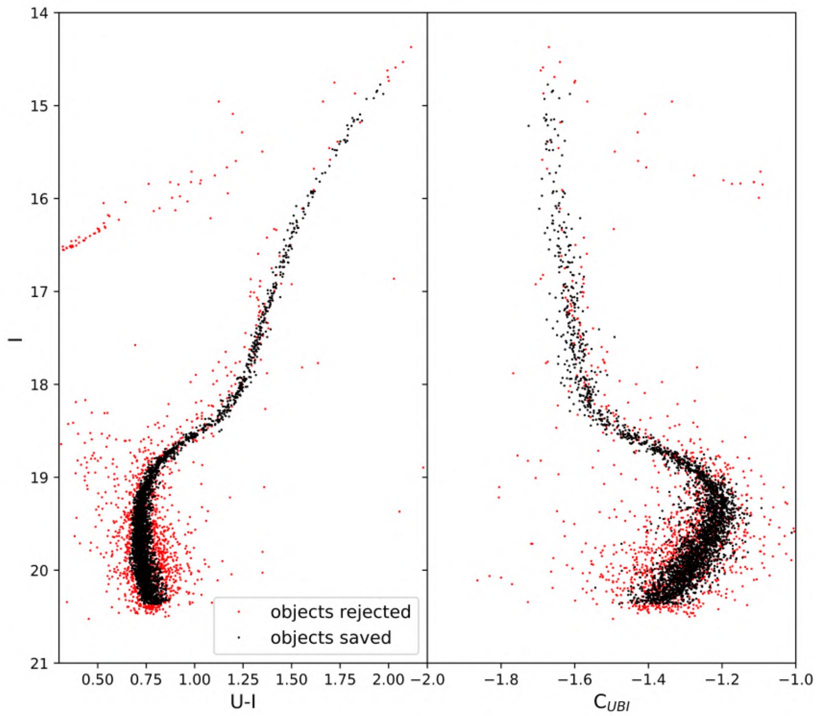

Figure 3.11: CMDs of NGC 5466 with rejected stars (in red) based on Figure 3.10. The right-hand panel shows CMD in C_{UBI} color index.

3.2.1 Selection of Multiple Populations

As for the previous cluster, we used ΔC_{UBI} and $\Delta(B-I)$ distribution to study multiple populations. The former one in **Figure 3.12** shows a quite blended bimodal distribution in the bottom right-hand panel, probing the presence of two populations in RGB. $\Delta(B-I)$ in **Figure 3.13** does not give a solid indication on the presence of two separate populations, with a steep Gaussian distribution of stars between the two fiducial ridgelines.

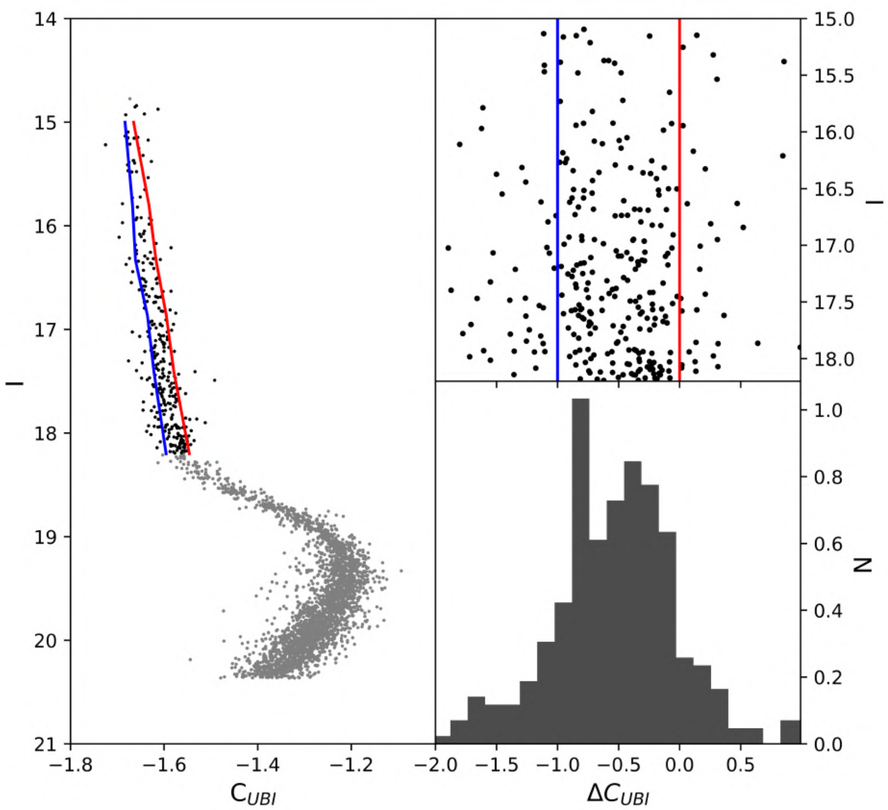

Figure 3.12: Left-hand panel: The C_{UBI} distribution of NGC 5466 stars in black on RGB, with the 4th percentile ridgeline in blue and the 96th percentile ridgeline in red. Right-hand panel: On top the resulting distribution ΔC_{UBI} of the same stars after normalization as described by equation (2.1). On bottom the distribution ΔC_{UBI} in terms of number of stars.

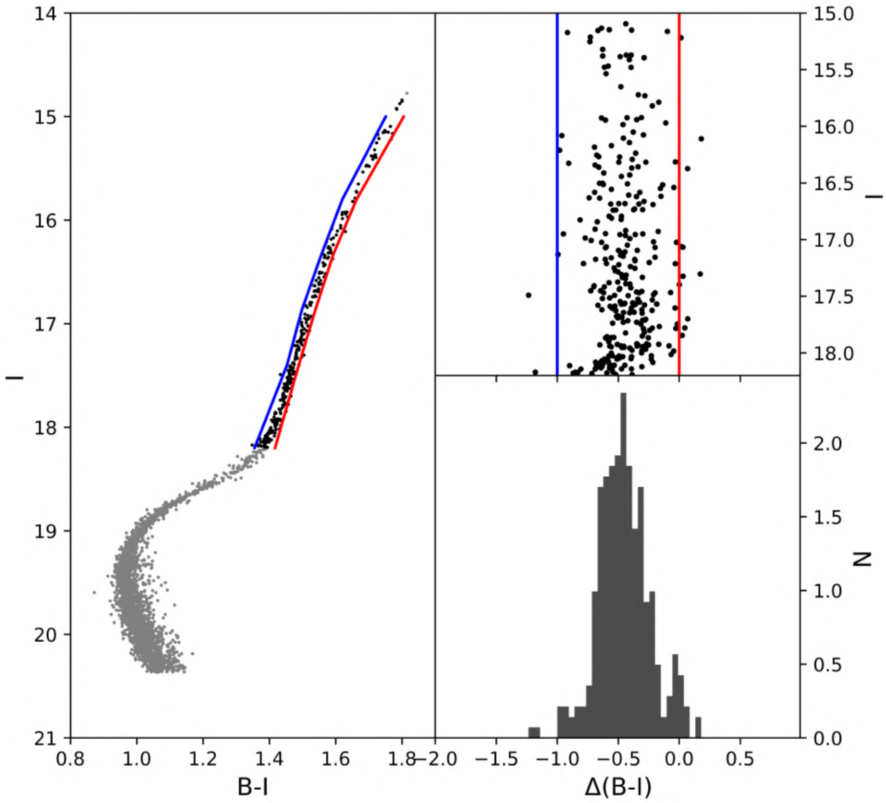

Figure 3.13: Left-hand panel: The (B-I) distribution of NGC 5466 stars in black on RGB, with the 4th percentile ridgeline in blue and the 96th percentile ridgeline in red. Right-hand panel: On top the resulting distribution $\Delta(B-I)$ of the same stars after normalization. On bottom the distribution $\Delta(B-I)$ in terms of number of stars.

To better distinguish the two populations, we performed a chromosome map considering ΔC_{UBI} and $\Delta(B-I)$ distributions (**Figure 3.14**). We noticed that the FG stars (in red ellipse) and SG stars (in blue ellipse) are less separated between each other by comparing this chromosome map to the one in Figure 3.7 using HST photometry. The plot shows a higher number of SG stars (169 versus 110) which are localized in a smaller region with respect to FG stars.

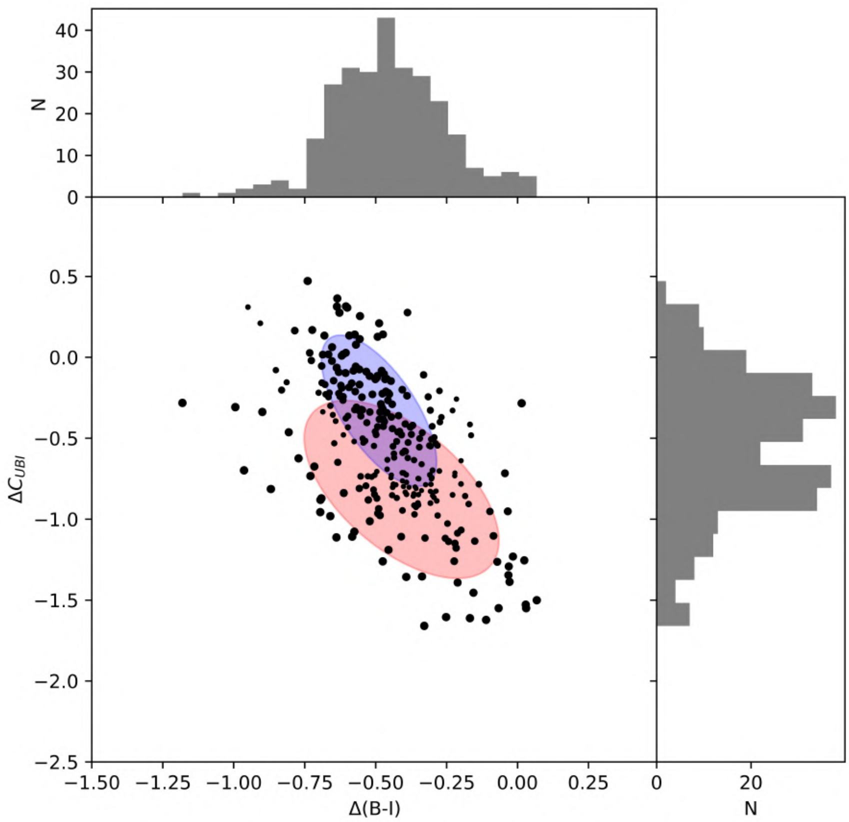

Figure 3.14: Chromosome map using Stetson for NGC 5466, with Gaussian Mixture Models (GMMs) applied in two dimensions. The lower left plot shows the chromosome map with populations P1 (red) and P2 (blue) as defined by the two distributions in the top and right-hand panels.

3.3 Results

In this section we combine together FG stars derived from HST and Stetson for NGC 5466, and the same we do for SG stars. Following section 2.4, we started the study of MPs with the cumulative radial distribution of the stars in each population.

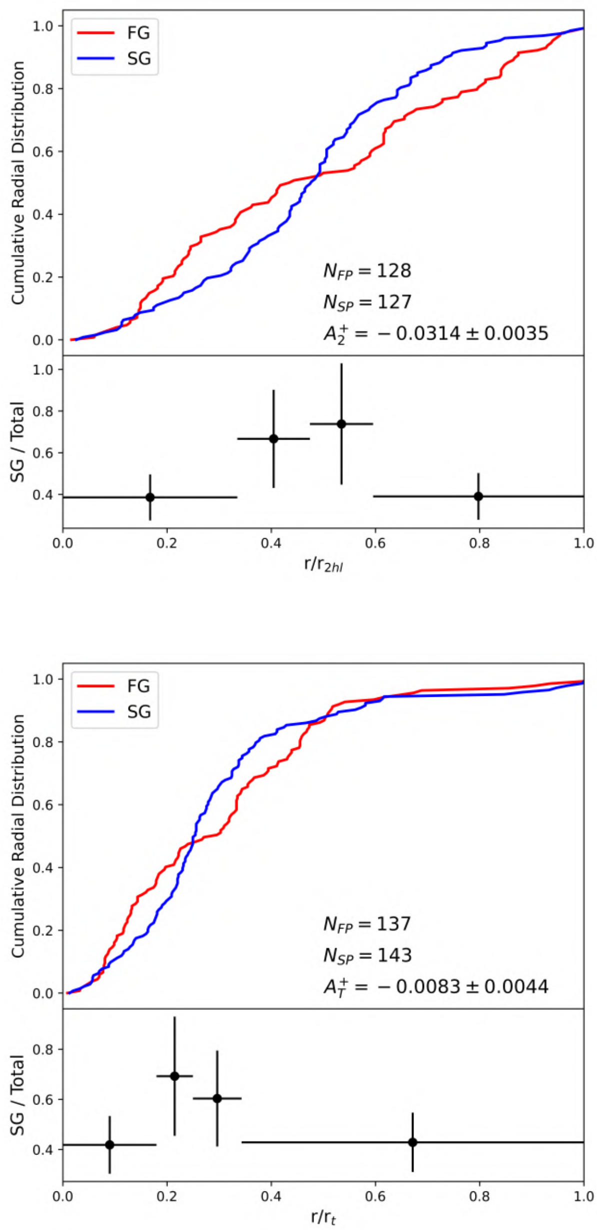

Figure 3.15: Top panels: Cumulative radial distribution of FG and SG stars up to $2R_{\rm HL}$ (upper plot) and $R_{\rm T}$ (lower plot). FG stars number($N_{\rm FP}$), SG stars number ($N_{\rm SP}$) and A^+ parameter are reported. Bottom panels: Radial distribution of SG stars over Total.

A^+ parameter (the difference between the areas below FG and SG cumulative radial distributions) is reported on each plot with the associated error. In the bottom panels we present the radial distribution of SG stars normalized to total. Within the first half of $2R_{\mathrm{HL}}$ FG dominates over SG, while in the second half SG assumes a steeper slope and overcome the cumulative radial distribution of FG. The steepness of SG increases mostly up to the first half of $2R_{\mathrm{HL}}$, hence the normalized number of SG stars has a peak at that level. Focusing on the cumulative distribution up to R_{T}, FG is more concentrated within the 20% of the projected radius, than SG dominates up to the first half. From now on, the two populations assume two cumulative radial distributions that overlap between each other several times. The normalized number distribution of SG stars has a peak when its cumulative radial distribution dominates, than the overlapping of the two populations creates big uncertainties in the measurement. As for NGC 5053, taken into account the errors, we can affirm that these two populations are dynamically mixed.

In order to better visualize the spatial distribution of MPs, we created 2-dimension plots centered in the center of NGC 5466. We highlighted FG and SG stars in two distinct panels (**Figure 3.16**), looking for relevant differences in their spatial distribution in inner and outer regions of the cluster.

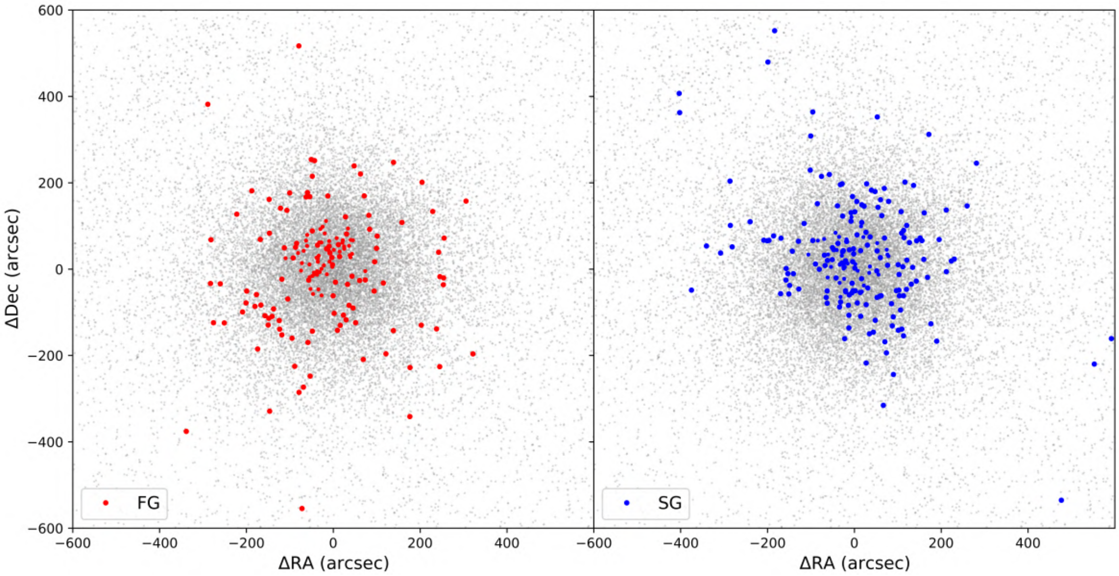

Figure 3.16: Spatial distribution of FG stars (left-hand panel, red dots) and SG stars(right-hand panel, blue dots) in NGC 5466.

SG stars seems to be more concentrated in the cluster center, while FG stars are more equally distributed at different radii. To better visualize this, we performed the 2-dimensional density map of FG and SG stars (**Figure 3.17**). The two populations present similar, homogeneous radial density distribution near the center. This confirmed the mixing scenario we saw also in NGC 5053, in contrast with other dynamically young GCs.

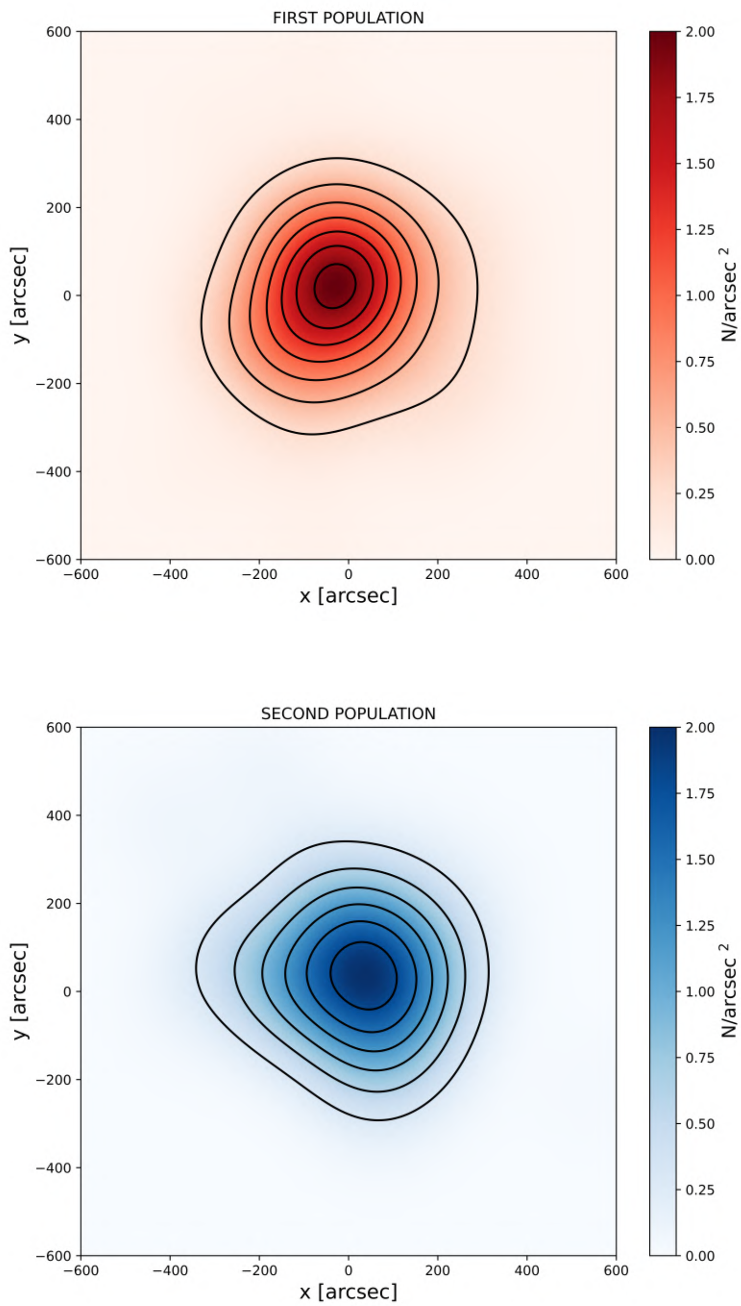

Figure 3.17: 2D density maps of FG stars (upper plot) and SG stars (lower plot) with contour lines in black. Density is color-coded by looking at the color bar on the right side of the two panels: dark color means high density region.

4 Conclusions

The overall results from this study show that both NGC 5053 and NGC 5466 present unattended mixed MPs in terms of spatial distribution. Hence, the scenario introduced by Dalessandro et al. (2019) and developed by further works where dynamically young GCs present a more centrally concentrated SG is not confirmed by these two clusters. Desipite being dynamically young, MPs in these clusters already went trough dynamical mixing, rising questions about the nature of processes that were able to produce this mix. In order to test the reliability of the derived FG and SG samples, in **Figure 4.1** we show the number of FG stars (divided by the total content of FG+SG stars) in relation with the mass of the clusters. Our results are consistent with the trend observed for the other clusters, where the mass is anti-correlated with the FG mass fraction. NGC 5053 and NGC 5466 are similar both in mass ($6.3{\cdot}10^4$ and $5.6{\cdot}10^4$ $M_\odot$) and in FG mass fraction (0.44 and 0.49), suggesting a common formation scenario.

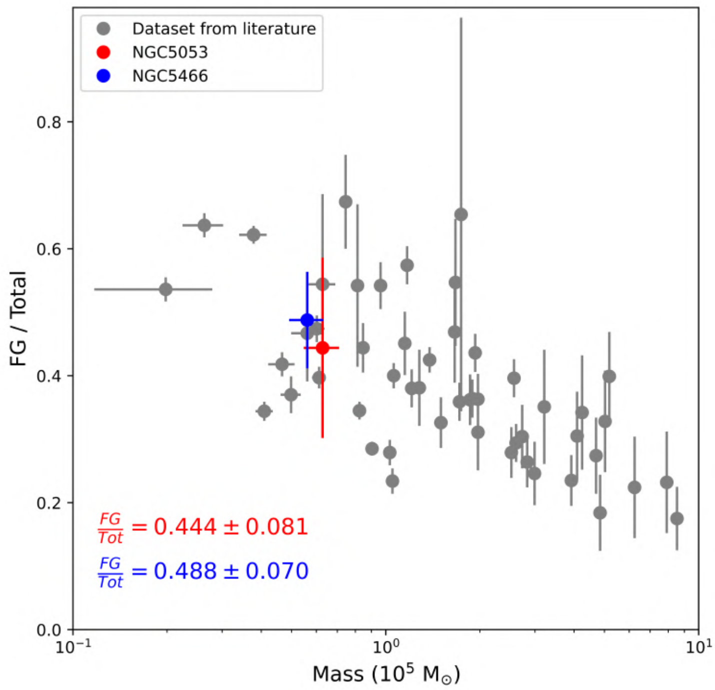

Figure 4.1: Relation between mass of the clusters and the number of their FG stars normalized by the total MP stars. Red and blue dots are our results which are compared to literature (grey dots). FG mass fractions are reported with the same color of the related dots.

We finally compare the cumulative radial distribution of MPs in NGC 5053 and NGC 5466 with the one of MPs in other dynamically young GCs reported by Dalessandro et al. (2019) (NGC 121, NGC 288, NGC 1978, NGC 5272 and NGC 6715) and by Onorato et al. (2023) (NGC 2419). We use the A^+ parameter, computed within twice the cluster half-light radius (A_2^+), as term of comparison between all the GCs. The left plot in **Figure 4.2** shows the relation between A_2^+ and mass of the clusters, while in the right plot A_2^+ is related with cluster central density (ρ_c). NGC 5053 and NGC 5466 assume the highest A_2^+ values ($A_2^+ \sim 0$), since all other clusters have negative A_2^+ due to more centrally concentrated P2, as expected from Dalessandro et al. (2019). At the same time, their masses and ρ_c are the smallest. All GCs follow this anti-correlated trend between A_2^+, which is a direct measure of MPs radial distribution, and structural parameters. In order to test the robustness of these relations, we derive the Spearman rank-order correlation coefficient, which is a nonparametric measure of the monotonicity of the relationship between two datasets. Spearman coefficient ~ -1 indicates an exact monotonic anti-correlation, while a value ~ 0 implies no correlation. For the A_2^+ - Mass relation, the Spearman coefficient is -0.9, indicating a solid anti-correlation between these two parameters. On the contrary, the Spearman coefficient for A_2^+ - ρ_c relation is -0.62, therefore there is a mild anti-correlation between MPs radial distribution and cluster central density. These intriguing relations should be studied in depth in order to find new ways to constrain MPs' dynamical and structural properties.

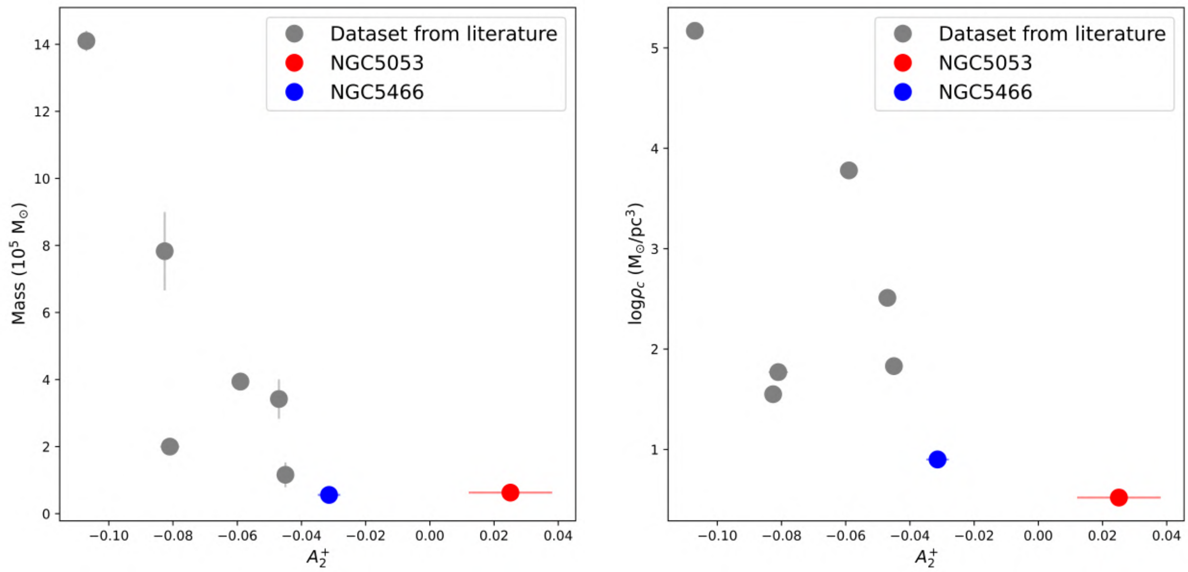

Figure 4.2: A_2^+ related to mass (left plot) and central density ρ_c (right plot) of six dynamically young GCs (grey dots) + NGC 5053 (red dot) and NGC 5466 (blue dot).

List of Figures

Bibliography

E. Alessandrini, B. Lanzoni, F. R. Ferraro, P. Miocchi, and E. Vesperini. *ApJ*, 833(2): 252, 2016.

A. Arellano Ferro, S. Giridhar, and D. M. Bramich. *MNRAS*, 402(1):226–244, 2010.

N. Bastian and C. Lardo. *Annu. Rev. Astron. Astrophys.*, 56:83–136, 2018.

N. Bastian, H. J. G. L. M. Lamers, S. E. de Mink, S. N. Longmore, S. P. Goodwin, and M. Gieles. *MNRAS*, 436(3):2398–2411, 2013.

H. Baumgardt, V. Hénault-Brunet, N. Dickson, and A. Sollima. Evidence for a bottom-light initial mass function in massive star clusters. *MNRAS*, 521(3):3991–4008, 2023.

G. Beccari, E. Dalessandro, B. Lanzoni, F. R. Ferraro, A. Sollima, M. Bellazzini, and P. Miocchi. *ApJ*, 776(1):60, 2013.

V. Belokurov, N. W. Evans, M. J. Irwin, P. C. Hewett, and M. I. Wilkinson. *ApJ*, 637 (1):L29–L32, 2006.

M. Cadelano, E. Dalessandro, and E. Vesperini. *A&A*, 685:A158, 2024.

E. Carretta, A. Bragaglia, R. G. Gratton, F. Leone, A. Recio-Blanco, and S. Lucatello. *A&A*, 450(2):523–533, 2006.

C. Charbonnel, W. Chantereau, M. Krause, F. Primas, and Y. Wang. *A&A*, 569:L6, 2014.

S.-H. Chun, J.-W. Kim, S. T. Sohn, J.-H. Park, W. Han, H.-I. Kim, Y.-W. Lee, M. G. Lee, S.-G. Lee, and Y.-J. Sohn. . *AJ*, 139(2):606–625, 2010.

E. Dalessandro, M. Cadelano, E. Vesperini, S. Martocchia, F. R. Ferraro, B. Lanzoni, N. Bastian, J. Hong, and N. Sanna. *ApJL*, 884(1):L24, 2019.

E. Dalessandro, M. Cadelano, A. Della Croce, F. I. Aros, E. B. White, E. Vesperini, C. Fanelli, F. R. Ferraro, B. Lanzoni, S. Leanza, and L. Origlia. *A&A*, 691:A94, 2024.

S. E. de Mink, O. R. Pols, N. Langer, and R. G. Izzard. *A&A*, 507(1):L1–L4, 2009.

T. Decressin, G. Meynet, C. Charbonnel, N. Prantzos, and S. Ekström. *A&A*, 464(3): 1029–1044, 2007.

S. G. Djorgovski and G. Meylan, editors. volume 50 of *Astronomical Society of the Pacific Conference Series*, 1993.

B. G. Elmegreen. *ApJ*, 836(1):80, 2017.

Gaia Collaboration. *A&A*, 674:A1, 2023.

M. Gieles, C. Charbonnel, M. G. H. Krause, V. Hénault-Brunet, O. Agertz, H. J. G. L. M. Lamers, N. Bastian, A. Gualandris, A. Zocchi, and J. A. Petts. *MNRAS*, 478(2):2461–2479, 2018.

R. G. Gratton, S. Lucatello, A. Sollima, E. Carretta, A. Bragaglia, Y. Momany, V. D'Orazi, S. Cassisi, and M. Salaris. *A&A*, 563:A13, 2014.

W. E. Harris. *AJ*, 112:1487, 1996.

P. F. Hopkins. *ApJ*, 797(1):59, 2014.

B. Lanzoni, F. R. Ferraro, E. Alessandrini, E. Dalessandro, E. Vesperini, and S. Raso. *ApJL*, 833(2):L29, 2016.

A. Lauchner, W. L. Powell, Jr., and R. Wilhelm. *ApJ*, 651(1):L33–L36, 2006.

E. Leitinger, H. Baumgardt, I. Cabrera-Ziri, M. Hilker, and E. Pancino. *MNRAS*, 520 (1):1456–1480, 2023.

M. Libralato, A. Bellini, E. Vesperini, G. Piotto, A. P. Milone, R. P. van der Marel, J. Anderson, A. Aparicio, B. Barbuy, L. R. Bedin, L. Borsato, S. Cassisi, E. Dalessandro, F. R. Ferraro, I. R. King, B. Lanzoni, D. Nardiello, S. Ortolani, A. Sarajedini, and S. T. Sohn. *ApJ*, 934(2):150, 2022.

A. Marcolini, B. K. Gibson, A. I. Karakas, and P. Sánchez-Blázquez. *MNRAS*, 395(2): 719–735, 2009.

A. Marín-Franch, A. Aparicio, G. Piotto, A. Rosenberg, B. Chaboyer, A. Sarajedini, M. Siegel, J. Anderson, L. R. Bedin, A. Dotter, M. Hempel, I. King, S. Majewski, A. P. Milone, N. Paust, and I. N. Reid. *ApJ*, 694(2):1498–1516, 2009.

A. P. Milone, A. F. Marino, G. Piotto, A. Renzini, L. R. Bedin, J. Anderson, S. Cassisi, F. D'Antona, A. Bellini, H. Jerjen, A. Pietrinferni, and P. Ventura. *ApJ*, 808(1):51, 2015.

A. P. Milone, G. Piotto, A. Renzini, A. F. Marino, L. R. Bedin, E. Vesperini, F. D'Antona, D. Nardiello, J. Anderson, I. R. King, D. Yong, A. Bellini, A. Aparicio, B. Barbuy, T. M. Brown, S. Cassisi, S. Ortolani, M. Salaris, A. Sarajedini, and R. P. van der Marel. *MNRAS*, 464(3):3636–3656, 2017.

M. Monelli, A. P. Milone, P. B. Stetson, A. F. Marino, S. Cassisi, A. del Pino Molina, M. Salaris, A. Aparicio, M. Asplund, F. Grundahl, G. Piotto, A. Weiss, R. Carrera, M. Cebrián, S. Murabito, A. Pietrinferni, and L. Sbordone. *MNRAS*, 431(3):2126–2149, 2013.

D. Nardiello, M. Libralato, G. Piotto, J. Anderson, A. Bellini, A. Aparicio, L. R. Bedin, S. Cassisi, V. Granata, I. R. King, F. Lucertini, A. F. Marino, A. P. Milone, S. Ortolani, I. Platais, and R. P. van der Marel. *MNRAS*, 481(3):3382–3393, 2018.

S. Onorato, M. Cadelano, E. Dalessandro, E. Vesperini, B. Lanzoni, and A. Mucciarelli. *A&A*, 677:A8, 2023.

W. Osborn. *The Observatory*, 91:223–224, 1971.

F. Pedregosa, G. Varoquaux, A. Gramfort, V. Michel, B. Thirion, O. Grisel, M. Blondel, A. Müller, J. Nothman, G. Louppe, P. Prettenhofer, R. Weiss, V. Dubourg, J. Vanderplas, A. Passos, D. Cournapeau, M. Brucher, M. Perrot, and É. Duchesnay. *Journal of Machine Learning Research*, 12:2825–2830, 2011.

G. Piotto, A. P. Milone, L. R. Bedin, J. Anderson, I. R. King, A. F. Marino, D. Nardiello, A. Aparicio, B. Barbuy, A. Bellini, T. M. Brown, S. Cassisi, A. M. Cool, A. Cunial, E. Dalessandro, F. D'Antona, F. R. Ferraro, S. Hidalgo, B. Lanzoni, M. Monelli, S. Ortolani, A. Renzini, M. Salaris, A. Sarajedini, R. P. van der Marel, E. Vesperini, and M. Zoccali. *AJ*, 149(3):91, 2015.

A. Renzini, A. F. Marino, and A. P. Milone. *MNRAS*, 513(2):2111–2117, 2022.

P. B. Stetson, E. Pancino, A. Zocchi, N. Sanna, and M. Monelli. *MNRAS*, 485(3):3042–3063, 2019.

A. J. Winter and C. J. Clarke. *MNRAS*, 521(2):1646–1673, 2023.

R. Wünsch, J. Palouš, G. Tenorio-Tagle, and S. Ehlerová. *ApJ*, 835(1):60, 2017.